

A Sonosensitizer-based Polymeric Nanoplatform for Realizing Chemo-sonodynamic Combination Therapy of Lung Cancer

Yanan Zhang

Shandong University

Abdur Rauf Khan

Shandong University

Xiaoye Yang

Shandong University

Yikang Shi

Shandong University

Xiaogang Zhao

Second Hospital of Shandong University Department of Ophthalmology

Guangxi Zhai (✉ professorgxzhai@126.com)

Shandong University

Research

Keywords: Chemo-sonodynamic therapy, Rhein, redox/enzyme/ultrasound responsive, reactive oxygen species, macrophages

Posted Date: December 1st, 2020

DOI: <https://doi.org/10.21203/rs.3.rs-113496/v1>

License:  This work is licensed under a Creative Commons Attribution 4.0 International License.

[Read Full License](#)

Version of Record: A version of this preprint was published on February 25th, 2021. See the published version at <https://doi.org/10.1186/s12951-021-00804-9>.

Abstract

Background

Lung cancer was regarded as the most common type of tumors worldwide, and the relative lethality was considerably high. However, since the tumor tissues located in deeper parts in human bodies, the traditional technologies like photodynamic therapy could not reach desired effect. Sonosensitizers can induce sonodynamic therapy, possessing the benefits of deep penetration and effective tumor inhibition by generating reactive oxygen. Besides, ultrasound possessed the ability of deep penetration, which showed favorable tumor inhibition effect.

Results

A redox/enzyme/ultrasound responsive Rhein-chondroitin sulfate nano-preparation encapsulating docetaxel was initially fabricated. The nanoparticles show increased cellular uptake with quick drug release, revealing good stability and monodispersed form in physiological environment. Also, Rhein could induce apoptosis and mitochondrial membrane potential change, enhancing the expression of [apoptosis-related protein](#). Further, the inhibited metastasis and angiogenesis of cancer cells by sonodynamic therapy would lead to reduced expression of M2 type macrophages.

Conclusion

Rhein was firstly discovered to possess the sonodynamic effect in this work by generating plenty of reactive oxygen after treating by ultrasound. The nanoparticle enhanced synergistic anti-tumor effect by both sonodynamic therapy and chemotherapeutic efficacy, and showed benign biocompatibility, which might pave a way for the investigation of chemo-sonodynamic therapy with different cancers.

Introduction

Lung cancer was deemed as a most frequently happened type of tumor-associated death worldwide. About 1.8 million people each year suffered from this disease with 88% lethality [1], and non-small cell lung cancer (NSCLC) occupied a dominant position [2, 3]. Among various nontherapeutic strategies, combination therapies based on multi-functional nanoparticle platforms are considered as an effective way to eliminate tumors nowadays [4, 5]. For example, the combination of sonodynamic therapy (SDT) and chemo-therapy has gained considerable attention [6].

To our best knowledge, the principle of SDT is similar to photodynamic therapy (PDT) via production of reactive oxygen species (ROS), leading to a singlet-to-triplet transition and apoptosis of tumor cells [7]. And ROS was investigated to initiate a mass of oxidization reactions and ultimately result in serious irreparable cellular damages [8]. In consideration of the low efficacy of ROS production by pure ultrasound, sonosensitizers (SSs) were applied to enhance the level of ROS with high selectivity [9]. Previously, SSs like protoporphyrin IX (PpIX) [10], hematoporphyrin monomethyl ether (HMME) [11],

chlorin e6 (Ce6) [12], titanium dioxide (TiO_2) [13] and Silicon-based [14] nanoparticles have all been investigated to produce ROS for tumor inhibition [15, 16], while these commonly used SSs were expensive and possessed SDT property only under ultrasonic condition. To overcome those difficulties, Rhein (Rh) was initially discovered to possess the SDT property in this work. Firstly, Rh was reported to gradually generate ROS by itself through JNK/Jun/caspase-3 signaling pathway, aggravating the ROS producing ability in deeper tissues beyond the reach of ultrasound [17]. Also, Rh exhibited favorable tumor inhibition to cancer cells through activating the secretion of apoptosis-related proteins such as caspase-3, BCL-2 and BAX [18], as well as inhibiting the tumor angiogenesis [19, 20]. However, the poor solubility and instability of Rh limited its effect in cancer suppression therapy, and it could not access to the tumor site accurately. Therefore, Rh was applied to construct a stimuli-responsive nanoplatform with better tumor inhibiting effect to A549 cells after applying ultrasound than free Rh.

Based on our previous work, chondroitin sulfate (CS), a family number of glycosaminoglycan with the ability to target CD44 receptors that were overexpressed on tumor cells, was selected as the backbone of nanoplatform[21–23]. Also, the latest research suggested that CS could target Golgi apparatus after cellular uptake process. Therefore, we combined Rh with CS using adipic dihydrazide (ADH) to aminate CS for formulating the stable amphiphilic polymer of CS-ADH-Rh. In addition, lipoic acid (LA) was also grafted in order to formulate intermolecular disulfide bonds and avoid the leaking problem. All the substance endowed the amphipathic self-assembled nanoplatform a sensitive switch to realize the control drug delivery when exposed to the highly reductive environment in cytoplasm [24–27]. In addition, the hydrophobic drug, docetaxel (DTX) with poor solubility and high toxicity, was applied and easily loaded into the hydrophobic segment of nanoplatform, which could play a role in combined therapy by inducing G2/M phase arrest in mitotic cell division and destroying microtubule structure of tumor cells [28, 29].

Consequently, we synthesized an ultrasound/redox/enzyme sensitive nanoplatform with CS-ADH-Rh-LA material, aiming at delivering Rh to cancer cells as well as curing with the help of SDT. The research found that Rh induced favorable SDT effect both *in vivo* and *in vitro*, and it exhibited good tumor inhibition efficiency. Besides, the encapsulation of DTX guaranteed the realization of combined chemo-sonodynamic therapy. Additionally, the organelle targeting property facilitated their damage especially on Golgi apparatus and mitochondria. The nanoparticles successfully enhanced ROS generation in time and concentration dependent ways after being ingested into A549 cells, and could powerfully inhibit the invasion and migration of cancer cells. The nanoplatform not merely improved the apoptosis inducing effect on tumor cells, but activated the body immune system after SDT treatment. Therefore, Rh as SSs was firstly discovered and applied in this nanoplatform with the advantages of high efficiency and economy, and provided a new thought for the development of novel SSs. Since the nanoplatform behaved favorable tumor suppression effect by itself and could regulate the systemic immune, their amphiphilic structure that enabled the encapsulation of other hydrophobic drugs and immune modulators, facilitating the combined therapy of multiple drugs.

Results And Discussion

Synthesis and characterization of nanoparticles

Nanoparticles with the material of CS-ADH-Rh-LA (NC-NPs and C-NPs representing the non-crosslinking and crosslinking nanoparticles) were prepared by simple sonication with the size ranging from 158.4 to 192.4 nm (Table 1). Although the Rh served as the hydrophobic part, the sizes of both NC-NPs and C-NPs increased with the increase of Rh to CS-ADH ratio, probably owing to the steric hindrance effect of Rh molecules. CMC value of NC-NPs with different ratios of Rh to CS-ADH was ranged from 33.74 to 66.54 µg/mL, which indicated excellent self-aggregation ability and dilution stability of NC-NPs (Table 1). Compared with NC-NPs, C-NPs had small size, more spherical shape and good dispersion (Fig. 1A and 1B), owing to their improved steadiness after crosslinking [30]. While both NC-NPs and C-NPs exhibited good stability with zeta potential of -28.9 mV and -30.9 mV, respectively (Table 1). In addition, the ¹H-NMR, ¹³C-NMR and FT-IR results of CS-ADH-Rh-LA were shown in Fig. S2.

Table 1
Characteristics of CS-Rh-LA nanoparticles. Values are listed as Mean ± SD, n = 3

NC-NPs				C-NPs				
Sample	Rh DS (%)	Diameter (nm)	PDI	ζ (mV)	CMC (µg/mL)	Diameter (nm)	PDI	ζ (mV)
CS-Rh-LA1	0.93	165.7 ± 4.23	0.153 ± 0.015	-15.6	66.54	138.5 ± 3.50	0.128 ± 0.018	-25.7
CS-Rh-LA2	2.69	180.6 ± 3.90	0.166 ± 0.029	-18.8	47.47	163.8 ± 3.09	0.122 ± 0.022	-26.8
CS-Rh-LA3	3.15	184.4 ± 2.50	0.100 ± 0.014	-21.0	33.74	178.3 ± 2.65	0.0913 ± 0.008	-28.9

Stability of nanoparticles

The stability of C-NPs was also evaluated when exposed to different concentrations of DTT solution (Fig. 1E). According to the result, the size of C-NPs increased from about 180.8 nm to 272.5 nm, 401.6 nm and 715.0 nm after 6, 12 and 24 h of incubation with 20 mM DTT solution, respectively, manifesting C-NPs swelled slightly and aggregated with crushed structure after 24 h incubation. Therefore, the monodispersed nanospheres changed into irregular stacks after 24 h as observed by TEM (Fig. 1C and 1D). However, there was negligible change in size of C-NPs incubated with 20 µM DTT solution (Fig. S3). In addition, there was little change in size of NC-NPs after incubating with DTT solutions. Further, *in vitro* stability was evaluated after incubating with PBS (pH7.4, 10 mM), NaCl and complete medium with 10% FBS for 24 h (Fig. 1F). In both PBS and NaCl solution, NC-NPs showed a decrease in size, while C-NPs

maintained favorable colloidal stability. Particularly, the stability of C-NPs was better than NC-NPs in 10% FBS solution within 6 days (Fig. S4). In addition, to estimate blood stability, the hemolysis rate of C-NPs was studied (Fig. 1G). Although the hemolysis rate was increased with the concentration of C-NPs but was below 5% in all contents (0.1 to 1 mg/mL), showing good biocompatibility of the synthesized polymers. Therefore, C-NPs possessed superior colloidal stability after crosslinking in normal physiological environment or blood, and disassembled quickly under simulative tumor microenvironment, guaranteeing their successful delivery.

Drug loading and release assay

To realize the combined therapy, DTX was encapsulated in C-NPs through sonication-dialysis method, and the effect of DTX to C-NPs ratio on drug loading was studied as shown in Table 2. As the raising of charge ratio (1:10 ~ 5:10), C-NPs could carry more DTX with the drug loading (DL%) rose from 2.50–12.05%. While corresponding encapsulate efficiency (EE%) increased from 23.93–35.73% as the ratio increased from 1:10 to 3:10, but at last reduced to 28.25% at 5:10 ratio, which could be explained by the breakage of hydrophobic-hydrophilic balance for superfluous addition of DTX. Besides, the size increased as the proportion of DTX increases, but the zeta potential showed the highest absolute value only at the ratio of 3:10. Over all the considerations, the 3:10 ratio of DTX to C-NPs was selected for further studies. After crosslinking, the *in vitro* release profile of DTX/C-NPs was evaluated in PBS solution containing 20 μM and 20 mM DTT, respectively (Fig. 1H). The cumulative release of DTX in PBS containing 20 mM DTT was more rapid in the first 12 h (nearly 80%) than the PBS containing 20 μM DTT and PBS without DTT, and reached to approximately 93% compared to 56% and 53% for 20 μM DTT or PBS group, respectively, at 72 h. Therefore, the drug delivery system could self-dissociate quickly and release the drug intelligently as the change of environment.

Table 2

Characteristics of DTX/CS-ADH-Rh-LA nanoparticles. All values are presented as Mean ± SD (n = 3)

Sample	DTX / polymer	DL (%)	EE (%)	Diameter (nm)	ζ (mV)
CS-ADH-Rh-LA	1 : 10	2.50 ± 0.18	23.93 ± 2.26	193.5 ± 1.2	-24.2
	2 : 10	5.71 ± 0.15	31.75 ± 2.11	201.7 ± 2.2	-25.2
	3 : 10	9.57 ± 0.38	35.73 ± 1.97	231.7 ± 3.9	-30.7
	5 : 10	12.05 ± 0.25	28.25 ± 1.37	254.0 ± 2.3	-28.9

Cellular uptake process

FCM and CLSM were used to analyze and observe the internalization of coumarin 6 (C6)-loaded C-NPs prepared by the same method of DTX/C-NPs. The fluorescent-labeled cells were screening out followed

by compiling the statistical data in histogram form (Fig. 2A). It was indicated that the C-NPs could internalize to A549 cells in time-dependent way as fluorescent signal became the strongest after 4 h of incubation. The signals for free coumarin group appeared in the same way, but the fluorescence intensity was much weaker than the C-NPs group. Meanwhile, the cellular uptake mechanism was studied using CLSM, as shown in Fig. 2C. In this part, the C6-loaded C-NPs were compared with free C6 and CS blocking group (A549 cells were treated with CS solutions in advance) at different time points. Similar to FCM result, the fluorescence of C6/C-NPs was fiercer than the C6 free group, while no signal was detected for the control group. The internalizing capacity of CS blocking group was between the control and free C6 group, manifesting successful blocking process of CD44 receptors and confirming the active targeting-mediated internalization of C-NPs. For H1299 cells, the fluorescence intensity was much weaker than the A549 cells on even ground (shown in Fig. 2D), confirming the abundance of CD44 receptors on A549 cells.

Further, the exocytosis-dependent transcellular transport of C6 loaded C-NPs was measured among disparate batches of A549 cells by means of simulation. According to Fig. S5, fluorescence intensity of C6 was high and visible in cells on coverslips (I) and (II), which indicated that certain C6 taken up at the first step was able to secrete into the new medium and then be taken as well as absorbing by cells on coverslip (II). However, the coverslip (III) showed scarcely fluorescent signal, which might be attributed to the reduction of fluorescent material. Collectively, C-NPs were actively taken up by cancer cells due to the overexpression of CD44 receptor, and the intake increased with time. Besides, the C-NPs were entered the cells via endocytosis and delivered to the surrounding cells through exocytosis, which might lay the foundation for active penetration, subsequently.

Cytotoxicity and apoptosis

The C-NPs- and DTX/C-NPs-induced cytotoxicity and apoptosis to A549 cells were evaluated. First, CCK-8 method was applied to estimate cytotoxicity of C-NPs to A549 cells. The cells were incubated with C-NPs at different concentration gradient of Rh, and ultrasound (1.2 W/cm²) was applied on those samples for 0, 1, 3 and 5 min (the groups were named as darkness, SDT-1, SDT-3 and SDT-5), respectively. According to the results, the C-NPs exhibited negligible cytotoxicity in dark environment at 0.1 µg/mL (Fig. 3A). While the dark cytotoxicity increased with the rise of Rh concentration and showed similar trend with those of SDT groups at 32 µg/mL concentration. However, the SDT groups exhibited significantly enhanced cytotoxicity ($p < 0.01$) in an ultrasonic time-dependent way. The IC₅₀ value was 1.061, 0.5664, 0.5049 and 0.2959 µg/mL for the dark, SDT-1 min, SDT-3 min and SDT-5 min groups, respectively. As manifested by Fig. 3B, C-NPs and DTX/C-NPs showed remarkable cell killing ability at low concentrations compared with free Rh under same environment, which probably attributed to the active targeting of the C-NPs. Besides, DTX/C-NPs manifested stronger cell killing effect after SDT treatment especially at low concentrations.

Further, the synergistic cytotoxicity of DTX/C-NPs against A549 and H1299 cells was studied (Fig. 3C and 3D). For A549 cells, DTX/C-NPs showed excellent cell killing effect even at low concentration of 10^{-3} $\mu\text{g}/\text{mL}$ in darkness with cell viability of 64.3% compared with H1299 cells of 93.8%, not to mention the SDT-treated groups. The results not only indicated the preferably active targeting of CS to CD44 receptors expressed on A549 cells rather than H1299 cells, but also the reduced cytotoxicity of DTX/C-NPs than free DTX solution (Fig. S6). Further, it could be deduced that cytotoxicity of C-NPs to was nearly doubled after encapsulating DTX with/without SDT treatment to A549 cells. In addition, the cell viability of CS-ADH-LA polymer was above 80% at all concentrations, exhibiting good safety (Fig. S7). Under the comprehensive consideration of effective cytotoxicity and shorter ultrasonic time, A549 cells and SDT for 3 min were applied for further experiments. Subsequently, the efficacy of DTX/C-NPs with SDT was evaluated through a live/dead-cell staining study with calcein-AM (ex/em: 490/515 nm) together with propidium iodide (PI) (ex/em: 517/617 nm) agents (Fig. 3E). The red fluorescence (dead cells) emerged and became stronger after incubating with DTX/C-NPs after SDT treatment compared with the control group, demonstrating their favorable ROS generating property. However, scarcely any red fluorescence was observed for free Rh group than Rh + SDT group, revealing good sonodynamic efficiency after SDT treatment for free Rh.

Merely ultrasound or Rh induced trivial apoptosis and necrosis to A549 cells (mortality ratio < 1%) according to the cell apoptosis result by FCM, and the apoptosis rate of SDT control group and CS-ADH-LA was similar (Fig. 3F). Besides, the mortality ratio of free Rh with SDT (6.9% of cell apoptosis rate) was enhanced than the control group, but far from DTX/C-NPs with SDT group (10.0% and 2.9% of cell apoptosis and necrotic rate). In addition, the stronger mortality ratio of Rh with SDT group than DTX/C-NPs group highlighted the importance of Rh as well as SDT treatment in tumor suppression in A549 cells, and the SDT induced distinct karyopyknosis and karyolysis compared with the group without SDT treatment at the same time point after culturing with DTX/C-NPs (Fig. 3G).

ROS detection during SDT process

The generation of ROS was considered crucial for the apoptosis and cellular components destruction of cancer cells [31], attributing to the addition of Rh with ultrasonic therapy and the consumption of GSH by NPs. The formation of intracellular ROS was detected in A549 cells using CLSM and FCM after different incubation times. Firstly, after 4 h, the Rh + SDT group manifested obvious green fluorescence compared with Rh group, and the fluorescence of NAC (ROS scavenger) and control group was negligible (Fig. S8). However, it was worth noting that Rh + SDT group and C-NPs + SDT group showed similar ROS producing capacity (Fig. S8 and Fig. 4A), which probably owing to the short incubation time that limited the ROS production. Then, to prove the correlation between effective SDT and intact structure of Rh, the singlet oxygen contents were detected with different agents using 9, 10-dimethylanthracene (DMA) after sonicating for 4 h. However, the peaks of Rh and C-NPs decreased fiercely compared with Ce6, EMO and the control group, and C-NPs generated even more singlet oxygen than C-NPs (Fig. 4B). Next, we observed the fluorescence image of ROS with different concentrations of C-NPs or various incubation times to

further verify the above hypothesis (Fig. 4C and Fig. 4D). To our anticipation, ROS was produced in a time and concentration dependent way. Nevertheless, fluorescence weakened at 5 µg/mL of C-NPs after 24 h incubation, which might be attributed to the apoptosis of A549 cells at such high concentration.

Detection of MMP

The change of MMP was the indication of destruction of Adenosine Triphosphate (ATP) producing process via utilizing the proton electrochemical gradient potential across the mitochondrial membrane [32]. We used jc-1 assay kit to determine the variation of MMP by FCM, and the y-axis and x-axis represented MMP in normal cells (red fluorescence) and abnormal cells (green fluorescence), respectively. The graph was divided into four parts, in which Q1 or Q4 represented pure fluorescence positive for red or green, while Q2 or Q3 as double positive or double negative, respectively. Control groups with/without SDT were located in Q1 zone predominantly, manifesting the formulation of jc-1 aggregates with high MMP level. However, the MMP was decreased in Rh + SDT and C-NPs + SDT groups, indicating the rupture of mitochondrial membrane and the dis-formable of jc-1 aggregates, and the destruction of mitochondrial membrane was aggravated with SDT time (Fig. 4E). According to the result, the green fluorescent ratio (sum of Q2 and Q4 zones) was 0.9% and 3.6% for control and control + SDT group, respectively, while increased to 30.6% and 49.4% for Rh and DTX/C-NPs groups after ultrasonication for 5 min. Therefore, ultrasound could damage the mitochondrial membrane, leading to cellular apoptosis in a time dependent way with the help of SSs.

DTX/C-NPs induces cell cycle arrest in A549 cells by facilitating microtubule polymerization

In order to study the growth inhibition effect of DTX/C-NPs to A549 cells, microtubule morphology and cell cycle were observed and analyzed. According to the result, the microtubule (marked by α-tubulin protein) had clear morphology and ran through the structure of A549 cells. However, the microtubule disappeared and formulated polymers on certain parts of A549 cells after culturing with DTX or DTX/C-NPs, manifesting the cytotoxicity and inhibition of cell division by DTX. Moreover, the SDT treatment facilitated the microtubule polymerization to a certain extent, though weak, as the images of control and Rh + SDT showed brighter red fluorescence in some parts of the cell (Fig. 5A). In addition, we investigated the influence of DTX/C-NPs to cell cycle arrest using a DNA detection kit with PI staining (Fig. 5C). Compared to control group, the percentage of G2/M increased from 21.06–23.20%, 25.76%, 60.88% and 62.01% for Rh + SDT, control + SDT, DTX and DTX/C-NPs + SDT groups, respectively. Therefore, A549 cells could be arrested in G2/M phase by promoting microtubule polymerization or preventing microtubule depolymerization with the help of DTX or DTX/C-NPs.

Western blot result

The apoptosis related proteins were measured via western blot assay (Fig. 5B). Since the apoptosis was related to poly ADP-ribose polymerase (PARP) cleavage, typical hallmarks of caspase-3 and activated

caspase-3 that were affirmed during the apoptosis were detected. Compared with the control group, DTX/C-NPs + SDT group expressed minimum amount of caspase-3 protein, but the maximum amount of cleaved caspase-3 protein. Additionally, the expression of MMP9 was also determined, which was regarded as an enzyme with the affinity to zinc, and could degrade the extracellular matrix as well as promote the invasion of cancer cells [33]. Besides, the expression of MMP9 decreased after incubating with DTX/C-NPs with/without SDT than control and Rh treated groups, proving the good anti-metastasis activity of DTX/C-NPs and SDT. However, there was little changes for VEGFA protein expression between different groups, manifesting the minimum effect of Rh in the inhibition of tumor angiogenesis with DTX/C-NPs or SDT at such a low concentration.

Subcellular localization and distribution

Subcellular localization and distribution were also studied by using C6/C-NPs. After staining with Lyso-Track Red, Mito-Tracker Red CMXRos and Golgi-Tracker Red mark for marking the lysosomes, mitochondria and Golgi apparatus, respectively, the cells were observed at different time points (Fig. 6). The results showed that only few signals of C6 colocalized with lysosomes and mitochondria, and their max Pearson correlation coefficients were 0.56 or 0.51 after incubating for 3 h, respectively (Fig. 6A, 6B, 6 Da and b). On the contrary, C-NPs rapidly colocalized with Golgi apparatus after the NPs was internalized into the cells for 1 h, and the Pearson correlation coefficient even reached to 0.92 (Fig. 6C and Fig. 6Dc). Therefore, it was preliminary speculated that the internalized C-NPs were transported to the Golgi apparatus within 1 h, and were gradually transferred to lysosome for further enzymolysis between 1 h and 3 h after the colocalization to Golgi membrane reached saturation. However, for mitochondria, the Pearson correlation coefficient had little difference for 1 h, 3 h and 6 h, but was significantly declined at 12 h, which might be attributed to the rupture of mitochondrial membrane after culturing for 12 h.

Destroy of Golgi structure

Since the Golgi apparatus was regarded as hub for sorting and trafficking of intracellular proteins, and could support cellular trafficking via balancing the of protein and membrane [34], the change in Golgi structures in connection with cancer disease was observed via immunofluorescent staining method. In our work, the stability of Golgi tethering protein GM130 (Golgi matrix protein) was investigated. The GM130 in DTX/C-NPs + SDT group showed obvious depolymerization as the number of red small spots were increased (Fig. 7A). Meanwhile, the small spots were counted and their average was calculated after incubating for 12 h (Fig. 7B). According to the result, the number of GM130 protein were in the sequence of Rh ≈ Control (+/-SDT) < DTX/C-NPs ≈ Rh (+ SDT) < DTX/C-NPs (+ SDT), manifesting the increasing disruption of Golgi structures among the groups that would lead to the increase of migration, invasion and poor prognosis of lung cancer [35].

Inhibition of cell migration and invasion

Since the migratory as well as invasive abilities are crucial to evaluate the metastatic cascade of cancer cells, the wound-healing assay together with the transwell invasion assay were performed in order to evaluate the migration and invasive ability on A549 cells with different solutions at their IC50

concentrations. According to the scratch test, the wound closure of control group could reach to 71.5% after 24 h, and changed to 67.1% after the SDT treatment. However, the rate was increased (75.5%) in C-NPs solution, but significantly reduced (34.9%) after SDT treatment, proving the inefficient migration inhibition of C-NPs to A549 cells. Besides, the values decreased to 62.6%, 52.7%, 32.9%, 27.5% and 15.8% for Rh, Rh + SDT, DTX, and DTX/C-NPs and DTX/C-NPs + SDT groups, respectively, manifesting the good anti-metastatic effect of SDT and DTX (include DTX/C-NPs) (Fig. 7C and 7D). We further investigated the invasive ability on the basis of migration assay, which showed a similar trend (Fig. 7E and 7F). The cell number was counted and the average cell number across the Matrigel was 227.4 ± 25.9 and 225.6 ± 25.6 for control and control + SDT groups. The C-NPs group showed similar invasion ability like the control one with cell number of 231.4 ± 23.8 , but the value decreased, significantly, after SDT to 106.2 ± 17.4 . As for DTX/C-NPs, the cell number showed persisting declination to 71.2 ± 9.4 and 33 ± 5.4 for DTX/C-NPs without and with SDT, respectively. Consequently, the SDT and DTX/C-NPs exhibited important roles in inhibiting cellular migration and invasion.

Biodistribution of Dir/C-NPs

In vivo imaging was conducted after injecting Dir (1,1-dioctadecyl-3,3,3,3-tetramethylindotricarbocyanineiodide)-loaded C-NPs or free Dir solution intravenously to the A549 tumor bearing nude mice at the time points of 1, 4, 12 and 24h, respectively. The whole mice bodies were scanned, photographed, and analyzed by the Caliper IVIS Lumina II system (Fig. 8A). At 1 h, the fluorescence signals of Dir reached to the maximum for both Dir/C-NPs and free Dir groups, manifesting the active targeting ability of C-NPs and quick distribution of Dir. However, the Dir signals weakened quickly in the free Dir group than Dir/C-NPs with the passage of time, owing to the long circulating ability of CS and active targeting of the nanoparticles compared with the rapid metabolism of free drug. After intravenous injection for 24 h, mice were executed and dissected to acquire their main organs for fluorometric analysis (Fig. 8B and 8C). Compared to the results of *in vivo* biodistribution images at 24 h, C-NPs exhibited strong fluorescence intensity after dissection especially in tumor tissues rather than the abdominal organs, owing to the abundant blood flow around the abdomen that facilitated the drug delivery. Therefore, the tumor tissues exhibited the greatest accumulations in Dir/C-NPs group, which was nearly 2.9-fold higher than the free Dir group, and the liver fluorescent intensity was 2.5-fold fold than the free Dir group.

Ex vivo tumor penetration

To estimate whether the ultrasound treatment could endow the redox/enzyme/ultrasound responsive self-destructive C-NPs a deep-penetrating ability, intact A549 solid tumors were dissected and incubated with C6/C-NPs with/without SDT treatment followed by frozen section. As depicted in Fig. 8D, ultrasound promoted the C6 penetration to deeper layers of A549 solid tumors by accelerating the blood flow in tumor vessels. For slices without SDT treatment, the C6 fluorescence was mainly observed at the surface of tumors with a narrow penetrating depth of $60.1 \mu\text{m}$, while the depth of C6 in SDT-treated tumors reached to $231.3 \mu\text{m}$ from the outer layers to the inner part. Further, the penetrating behavior was quantitatively described by Image J software. Two lines were drawn from the surface of tumor slices to

the inner layers, and the fluorescent intensity along with the lines was plotted at different distance from the outer layer of tumors (Fig. 8E). The signal attenuation trends of C6 in C-NPs were in line with the fluorescent result, suggesting the penetration promoting effect of ultrasound in tumor cells.

Anti-tumor efficiency

The *in vivo* anti-tumor of DTX/C-NPs by bilateral A549 tumor-bearing mice models was evaluated (Fig. 9A). The relative tumor volume (RTV) of bilateral tumor-bearing mice ('Right (R)' for *in situ* tumors and 'Left (L)' for distal tumors) was measured, and the body weight changes were also recorded (Fig. 9B to 9D). Conceivably, the tumor suppression effect was similar for 'R' and 'L' tumors, and the DTX/C-NPs with/without SDT groups showed decrescent RTV after 14 days compared with the control group (NS) with RTV of 4.40, 3.94, 1.62, 1.28, 0.74 and 0.77 for NS (R), NS (L), DTX/C-NPs (R), DTX/C-NPs (L), DTX/C-NPs + SDT (R) and DTX/C-NPs + SDT (L), respectively. Whereas, the C-NPs groups exhibited considerably lower RTV compared with Taxotere® and DTX + Rh groups especially for the L tumors in C-NPs group, which was probably contributed to the smaller size of distal tumors (Fig. 9E). Subsequently, the body weights of mice except for the groups of Taxotere® and DTX + Rh exhibited no significant change compared with NS group. The curves of Taxotere® and DTX + Rh showed that mice gained the minimum body weights at day 10 but regained the loss after the administration stopped. Therefore, the free drug possessed cumulative toxicity to mice, but could be metabolized quickly at the end of the administration.

Further, the expressions of COX-2 and uPA proteins in 'L' tumor tissues was evaluated via western blot assay with for observing the tumor metastasis-related indicators by preparing the homogenate (Fig. 9F). The expression of both COX-2 and uPA proteins was decreased in C-NP + SDT and DTX/C-NPs + SDT groups compared with NS group, manifesting the good anti-metastatic effect of the SDT and chemo-sonodynamic combined treatment. Meanwhile, H&E staining assay was conducted and showed no obvious pathological damage of the main organs of (Fig. S9). Additionally, all 'R' and 'L' tumors were stained with H&E staining, and the slices images showed wonderful pro-apoptotic effect with a small amount of blue nucleus in DTX/C-NPs and DTX/C-NPs + SDT groups. Besides, C-NPs + SDT also presented reduced nucleus compared with NS group. However, the pro-apoptotic effect of SDT and combined therapy for 'L' tumors was less distinct than the 'R' results (Fig. 9G and 9H). TUNEL assay showed similar results both for 'R' and 'L' tumors (Fig. 9I and Fig. S10).

Figure 9 The summary of *in vivo* anti-tumor effect with bilateral A549 mice model. (A) Overall schedule of *in vivo* tumor inhibition study. RTV curves of 'R' (B) and 'L' (C) tumors and body weight curves (D). (E) Photographs of 'R' and 'L' tumors after the autopsy. (F) Western blot result of COX-2 and uPA proteins expression after treatment with different solutions at day 15. H&E stained images of 'R' (G) and 'L' (H) tumor tissues after the treatment with NS, C-NPs (SDT+), Taxotere, DTX + Rh, DTX/C-NPs (SDT + or SDT-). Scar bar, 100 µm. (I) TUNEL results of 'R' tumor from all bilateral tumor-bearing mice treated with NS, C-NPs (SDT+), Taxotere, DTX + Rh, DTX/C-NPs (SDT + or SDT-). Scar bar, 100 µm. ** $p < 0.01$, *** $p < 0.001$.

The apoptotic cells were stained with yellow or pale brown color and signed by red arrows or curves, while the normal cells were presented as blue nuclei. According to the result, the NS showed negligible tumor apoptosis, while SDT induced powerful cellular apoptosis observed by the larger brown areas in the slices. The synergetic therapy of DTX/C-NPs + SDT was the most effective in cell killing as seen from the large number of brown vacuoles with several apoptotic nuclei among them, but DTX/C-NPs group showed feeble efficacy. Moreover, the tumor tissues in DTX + Rh group exhibited more apoptosis than Taxotere® group owing to the little production of ROS by the Rh.

Serum composition detection

Considering the RTV and H&E staining results for 'R' and 'L' tumors, it was speculated that the immune system of mice might be activated during the course of administration after SDT treatment. Thus, the serum composition of IL-10 and IL-12 was measured by Elisa kit aiming at evaluating the generation of M2 and M1 subtypes of macrophages that acted as the pro/anti-inflammatory cytokines after different treatment [36]. Results suggested that the IL-10 content decreased after SDT treatment with C-NPs or DTX/C-NPs, however the variation was on the opposite side for the IL-12 factor (Fig. 10A). Therefore, SDT could elevate the expression of M1 macrophages while decrease the M2 type, manifesting the effective enhancement in the immune capacity of macrophages of DTX/C-NPs group with the help of ultrasound. In addition, the serum biochemical indicators of ALT, AST, CREA and BUN were detected (Fig. 10B to 10D), and the result implied no significant differences among different treating groups, indicating the good safety to heart, liver or kidney of DTX/C-NPs + SDT administration.

Immunocytochemical staining

Based on the disparate result of Fig. 5B (expression of MMP9 and VEGFA proteins), the immunofluorescence technique was applied to the 'L' tumor tissues with anti-CD31 marker to make clear that whether the angiogenesis in tumors was inhibited after SDT treatment (Fig. 10E). The endothelial cells in platelet, shown as red fluorescence in the slices, disappeared after C-NPs + SDT, DTX/C-NPs and DTX/C-NPs + SDT treatment than the NS group, manifesting the good vascular inhibition effect of DTX/C-NPs and SDT. Thus, the angiogenesis was indeed inhibited after DTX/C-NPs + SDT treatment but not through the VEGFA pathway. In addition, the M2 macrophages in tumor tissues were also stained with anti-CD206 marker and imaged. In accord with the histogram in IL-10 factor, lesser M2 macrophages were produced after SDT treatment compared with the other groups as the green fluorescence increased.

Conclusion

We have synthesized an active tumor targeting nanoplatform based on DTX/C-NPs and SDT via covalent bonds by realizing combined chemo-sonodynamic therapy. Using LA to formulate the intermolecular disulfide bonds after crosslinking, together with Rh as SSs that applied for the first time, well realized the redox /enzyme /ultrasound responsive property of the nanoparticles with low price. The DTX/C-NPs not only enhanced the solubility and cellular uptake ability of DTX, but decreased its violent toxicity to normal cells. Except for the innate ability to produce ROS of Rh in tumor cells, the SDT effect that enhanced the

generation of ROS significantly aggravated the tumor inhibition efficacy to cancer cells in time and concentration dependent ways after ultrasonic treatment. Further, DTX/C-NPs also showed good organelle targeting ability to Golgi apparatus and mitochondria, leading to the destruction of their structures after SDT treatment. On account of the encapsulation of DTX, the nanoparticles efficaciously changed the microtubule morphology and blocked the mitotic cycle of A549 cancer cells with significantly reduced the toxicity of free DTX. Benefiting from deep penetration after ultrasound treatment, the DTX/C-NPs entered into deeper tumor tissues and exhibited favorable tumor growth suppression effect with good safety. Meanwhile, the immune system in mice were obviously activated after SDT by expressing lesser M2 type macrophages while improving the formation of M1 type macrophages, and the angiogenesis of tumor vessels was inhibited at the same time.

Declarations

Availability of data and materials

All data generated or analyzed during this are included in this published article

Acknowledgements

We thank Jianbo Ji and Huixian Yan from Shandong University for their help on animal surgery.

Funding

This work acquired the financial support from the Major Research Project of Shandong Province, P.R.China (No.2018GSF118004), Shandong Provincial Major Science &Technology Innovation Project, P.R.China (No.2018CXGC1411) and Major Basic Research Projects of Shandong Natural Science Foundation, P.R.China (No. ZR2018ZC0232).

Author Contributions

YZ, XY and GZ contributed to conception. YZ, XZ and GZ contributed to the research design. YZ and XY contributed to data acquisition. YZ and XY contributed to article writing. GZ contributed to review and editing. YS contributed to the cell experiment. All authors read and approved the final manuscript.

Ethics declarations

Ethics approval and consent to participate

Animal experiment was conducted following guidelines of Institutional Animal Care and Use Committee.

Consent for publication

Not applicable.

Competing interests

The authors declare no conflict of interests in the paper.

References

1. Hirsch FR, Scagliotti GV, Mulshine JL, Kwon R, Curran WJ et al. Lung cancer: current therapies and new targeted treatments. *The Lancet*. 2017;389(10066):299-311. [https://doi.org/10.1016/s0140-6736\(16\)30958-8](https://doi.org/10.1016/s0140-6736(16)30958-8)
2. Califano R, Gomes F, Ackermann CJ, Rafee S, Tsakonas G et al. Immune checkpoint blockade for non-small cell lung cancer: What is the role in the special populations? *Eur J Cancer*. 2020;125(1-11). <https://doi.org/10.1016/j.ejca.2019.11.010>
3. Arbour KC; Riely GJ. Systemic Therapy for Locally Advanced and Metastatic Non-Small Cell Lung Cancer: A Review. *JAMA*. 2019;322(8):764-774. <https://doi.org/10.1001/jama.2019.11058>
4. Vijayaraghavalu S, Gao Y, Rahman MT, Rozic R, Sharifi N et al. Synergistic combination treatment to break cross talk between cancer cells and bone cells to inhibit progression of bone metastasis. *Biomaterials*. 2020;227(119558). <https://doi.org/10.1016/j.biomaterials.2019.119558>
5. Liu M, Khan AR, Ji J, Lin G, Zhao X et al. Crosslinked self-assembled nanoparticles for chemo-sonodynamic combination therapy favoring antitumor, antimetastasis management and immune responses. *Journal of Controlled Release*. 2018;290(150-164). <https://doi.org/10.1016/j.jconrel.2018.10.007>
6. Zheng X, Liu W, Ge J, Jia Q, Nan F et al. Biodegradable Natural Product-Based Nanoparticles for Near-Infrared Fluorescence Imaging-Guided Sonodynamic Therapy. *ACS Appl Mater Interfaces*. 2019;11(20):18178-18185. <https://doi.org/10.1021/acsami.9b03270>
7. Wu W, Mao D, Hu F, Xu S, Chen C et al. A Highly Efficient and Photostable Photosensitizer with Near-Infrared Aggregation-Induced Emission for Image-Guided Photodynamic Anticancer Therapy. *Adv Mater*. 2017;29(33). <https://doi.org/10.1002/adma.201700548>
8. Song D, Yue W, Li Z, Li J, Zhao J et al. Study of the mechanism of sonodynamic therapy in a rat glioma model. *Onco Targets Ther*. 2014;7(1801-10). <https://doi.org/10.2147/OTT.S52426>
9. Wang P, Zhou F, Guan K, Wang Y, Fu X et al. In vivo therapeutic response monitoring by a self-reporting upconverting covalent organic framework nanoplatform. *Chemical Science*. 2020;11(5):1299-1306. <https://doi.org/10.1039/c9sc04875h>
10. Zhang Q, Wang N, Ma M, Luo Y; Chen H. Transferrin Receptor-Mediated Sequential Intercellular Nanoparticles Relay for Tumor Deep Penetration and Sonodynamic Therapy. *Advanced*

- Therapeutics. 2019;2(6):1800152. <https://doi.org/10.1002/adtp.201800152>
11. Huang J,Liu F,Han X,Zhang L,Hu Z et al. Nanosonosensitizers for Highly Efficient Sonodynamic Cancer Theranostics. *Theranostics*. 2018;8(22):6178-6194. <https://doi.org/10.7150/thno.29569>
12. Yang ZL,Tian W,Wang Q,Zhao Y,Zhang YL et al. Oxygen-Evolving Mesoporous Organosilica Coated Prussian Blue Nanoplatform for Highly Efficient Photodynamic Therapy of Tumors. *Adv Sci (Weinh)*. 2018;5(5):1700847. <https://doi.org/10.1002/advs.201700847>
13. Hu C,Huang HW,Chen F,Zhang YH,Yu H et al. Coupling Piezocatalysis and Photocatalysis in Bi₄NbO₈X (X = Cl, Br) Polar Single Crystals. *Advanced Functional Materials*. 2020;30(7). <https://doi.org/10.1002/adfm.201908168>
14. Singh J,Jadhav S,Avasthi S; Sen P. Designing Photocatalytic Nanostructured Antibacterial Surfaces: Why Is Black Silica Better than Black Silicon? *ACS Appl Mater Interfaces*. 2020;12(18):20202-20213. <https://doi.org/10.1021/acsami.0c02854>
15. Wu M,Ding Y; Li L. Recent progress in the augmentation of reactive species with nanoplatforms for cancer therapy. *Nanoscale*. 2019;11(42):19658-19683. <https://doi.org/10.1039/c9nr06651a>
16. Qian X,Zheng Y; Chen Y. Micro/Nanoparticle-Augmented Sonodynamic Therapy (SDT): Breaking the Depth Shallow of Photoactivation. *Adv Mater*. 2016;28(37):8097-8129. <https://doi.org/10.1002/adma.201602012>
17. Li-Weber M. Targeting apoptosis pathways in cancer by Chinese medicine. *Cancer Lett*. 2013;332(2):304-12. <https://doi.org/10.1016/j.canlet.2010.07.015>
18. Yang L,Lin S,Kang Y,Xiang Y,Xu L et al. Rhein sensitizes human pancreatic cancer cells to EGFR inhibitors by inhibiting STAT3 pathway. *J Exp Clin Cancer Res*. 2019;38(1):31. <https://doi.org/10.1186/s13046-018-1015-9>
19. Wang A,Jiang H,Liu Y,Chen J,Zhou X et al. Rhein induces liver cancer cells apoptosis via activating ROS-dependent JNK/Jun/caspase-3 signaling pathway. *J Cancer*. 2020;11(2):500-507. <https://doi.org/10.7150/jca.30381>
20. Hu L,Cui R,Liu H; Wang F. Emodin and rhein decrease levels of hypoxia-inducible factor-1a in human pancreatic cancer cells and attenuate cancer cachexia in athymic mice carrying these cells. *Oncotarget*. 2017;8(50). <https://doi.org/>,
21. Jardim KV,Siqueira JLN,Bao SN,Sousa MH; Parize AL. The role of the lecithin addition in the properties and cytotoxic activity of chitosan and chondroitin sulfate nanoparticles containing curcumin. *Carbohydr Polym*. 2020;227(115351). <https://doi.org/10.1016/j.carbpol.2019.115351>
22. Xie C,Wang Q,Ying R,Wang Y,Wang Z et al. Binding a chondroitin sulfate-based nanocomplex with kappa-carrageenan to enhance the stability of anthocyanins. *Food Hydrocolloids*. 2020;100(105448). <https://doi.org/10.1016/j.foodhyd.2019.105448>
23. Zhang X,Ma Y,Ma L,Zu M,Song H et al. Oral administration of chondroitin sulfate-functionalized nanoparticles for colonic macrophage-targeted drug delivery. *Carbohydr Polym*. 2019;223(115126). <https://doi.org/10.1016/j.carbpol.2019.115126>

24. Liao C,Dai X,Chen Y,Liu J,Yao Y et al. Biogenic (R)-(+)-Lipoic Acid Only Constructed Cross-Linked Vesicles with Synergistic Anticancer Potency. *Advanced Functional Materials*. 2019;29(3):1806567. <https://doi.org/10.1002/adfm.201806567>
25. Huang J,Wang L,Zhao P,Xiang F,Liu J et al. Nanocopper-Doped Cross-Linked Lipoic Acid Nanoparticles for Morphology-Dependent Intracellular Catalysis. *ACS Catalysis*. 2018;8(7):5941-5946. <https://doi.org/10.1021/acscatal.8b01337>
26. Yang Y,Zhu H,Wang J,Fang Q; Peng Z. Enzymatically Disulfide-Crosslinked Chitosan/Hyaluronic Acid Layer-by-Layer Self-Assembled Microcapsules for Redox-Responsive Controlled Release of Protein. *ACS Appl Mater Interfaces*. 2018;10(39):33493-33506. <https://doi.org/10.1021/acsami.8b07120>
27. Li A; Zhang D. Synthesis and Characterization of Cleavable Core-Cross-Linked Micelles Based on Amphiphilic Block Copolypeptoids as Smart Drug Carriers. *Biomacromolecules*. 2016;17(3):852-61. <https://doi.org/10.1021/acs.biomac.5b01561>
28. Li L,Sun W,Zhang Z; Huang Y. Time-staggered delivery of docetaxel and H1-S6A,F8A peptide for sequential dual-strike chemotherapy through tumor priming and nuclear targeting. *Journal of Controlled Release*. 2016;232(62-74). <https://doi.org/10.1016/j.jconrel.2016.04.021>
29. Zhou H,Lv S,Zhang D,Deng M,Zhang X et al. A polypeptide based podophyllotoxin conjugate for the treatment of multi drug resistant breast cancer with enhanced efficiency and minimal toxicity. *Acta Biomater*. 2018;73(388-399). <https://doi.org/10.1016/j.actbio.2018.04.016>
30. Trinh T,Liao C,Toader V,Barlog M,Bazzi HS et al. DNA-imprinted polymer nanoparticles with monodispersity and prescribed DNA-strand patterns. *Nat Chem*. 2018;10(2):184-192. <https://doi.org/10.1038/nchem.2893>
31. Yao C,Wang W,Wang P,Zhao M,Li X et al. Near-Infrared Upconversion Mesoporous Cerium Oxide Hollow Biophotocatalyst for Concurrent pH/H₂O₂-Responsive O₂-Evolving Synergetic Cancer Therapy. *Adv Mater*. 2018;30(7). <https://doi.org/10.1002/adma.201704833>
32. Gao M,Yi J,Zhu J,Minikes AM,Monian P et al. Role of Mitochondria in Ferroptosis. *Mol Cell*. 2019;73(2):354-363 e3. <https://doi.org/10.1016/j.molcel.2018.10.042>
33. Ma T,Hou Y,Zeng J,Liu C,Zhang P et al. Dual-Ratiometric Target-Triggered Fluorescent Probe for Simultaneous Quantitative Visualization of Tumor Microenvironment Protease Activity and pH in Vivo. *J Am Chem Soc*. 2018;140(1):211-218. <https://doi.org/10.1021/jacs.7b08900>
34. Gao H,Xie W,Yang C,Xu J,Li J et al. NRAMP2, a trans-Golgi network-localized manganese transporter, is required for *Arabidopsis* root growth under manganese deficiency. *New Phytol*. 2018;217(1):179-193. <https://doi.org/10.1111/nph.14783>
35. Eisenberg-Lerner A,Benyair R,Hizkiahou N,Nudel N,Maor R et al. Golgi organization is regulated by proteasomal degradation. *Nat Commun*. 2020;11(1):409. <https://doi.org/10.1038/s41467-019-14038-9>
36. Larionova I,Kazakova E,Patysheva M; Kzhyshkowska J. Transcriptional, Epigenetic and Metabolic Programming of Tumor-Associated Macrophages. *Cancers (Basel)*. 2020;12(6). <https://doi.org/10.3390/cancers12061411>

Figures

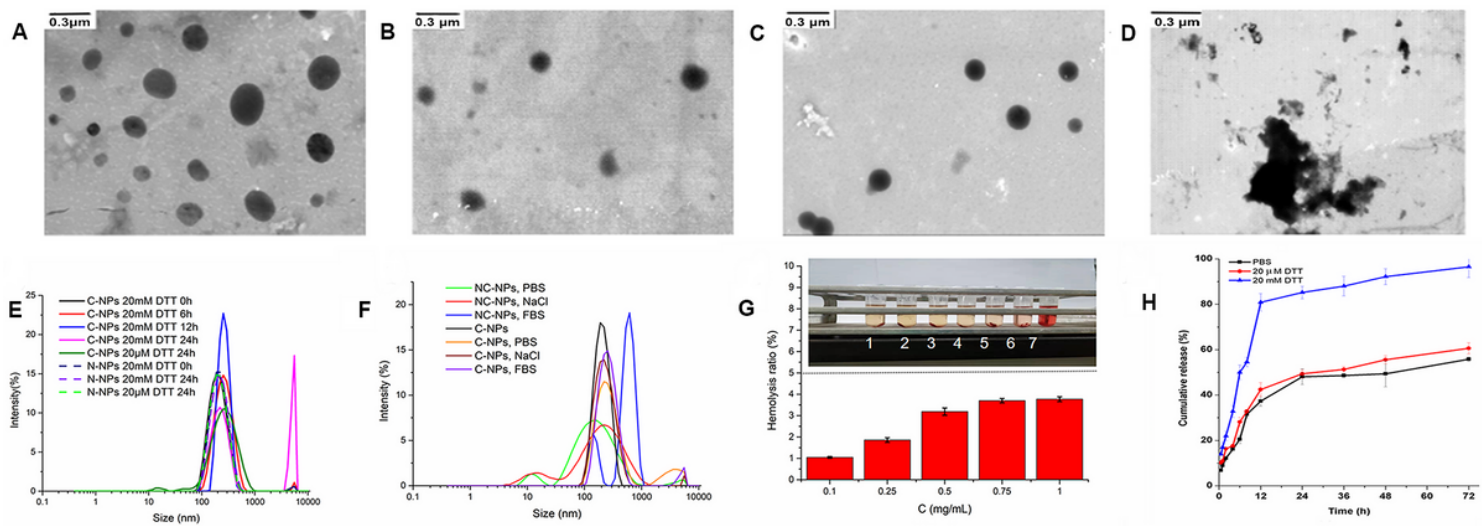


Figure 1

The morphology of NC-NPs (A) and C-NPs dispersed in DW (B) observed by TEM. The particle size distribution of C-NPs after 24h of incubation with 20 μ M DTT (C) and 20 mM DTT (D). (E) The responsive disassembly of C-NPs and NC-NPs. Particle size was determined at different time points in reductive environment under the existence of DTT. (F) Crosslinking stability of nanoparticles. Size changes of C-NPs and NC-NPs in various solutions of PBS, NaCl and 10% FBS. (G) Hemolysis rate of C-NPs (number 1-7 represents the groups of blank control, 0.1, 0.25, 0.5, 0.75, 1 mg/mL C-NPs and positive control). (H) Cumulative DTX release study from the C-NPs. * $p < 0.05$, ** $p < 0.01$.

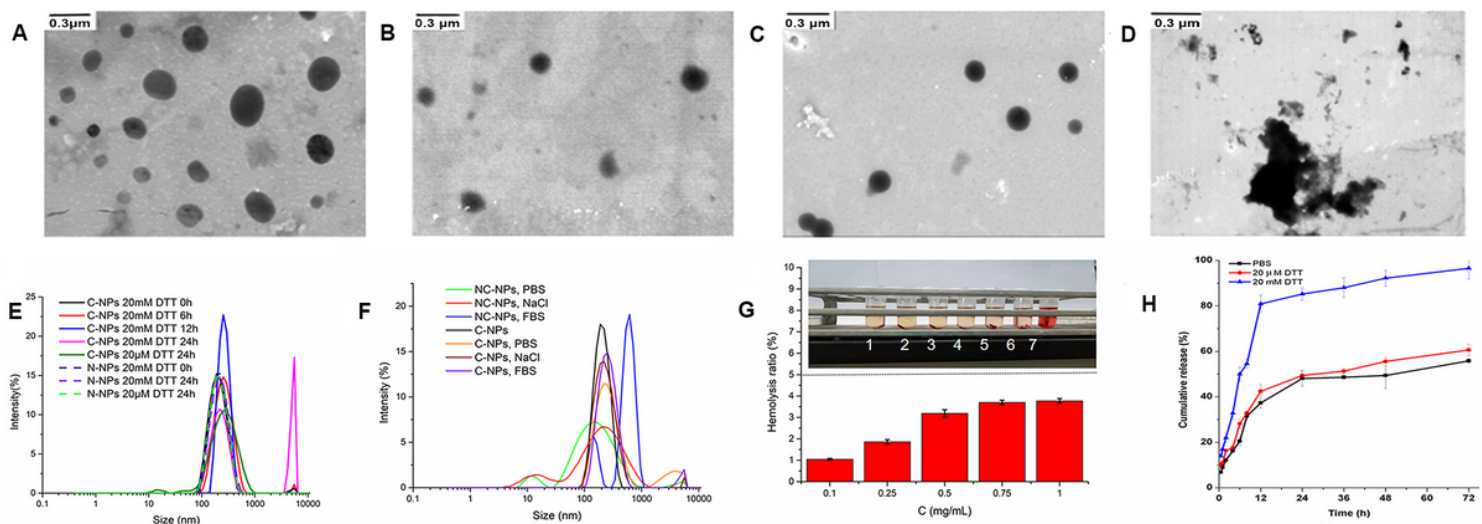


Figure 1

The morphology of NC-NPs (A) and C-NPs dispersed in DW (B) observed by TEM. The particle size distribution of C-NPs after 24h of incubation with 20 μ M DTT (C) and 20 mM DTT (D). (E) The responsive disassembly of C-NPs and NC-NPs. Particle size was determined at different time points in reductive

environment under the existence of DTT. (F) Crosslinking stability of nanoparticles. Size changes of C-NPs and NC-NPs in various solutions of PBS, NaCl and 10% FBS. (G) Hemolysis rate of C-NPs (number 1-7 represents the groups of blank control, 0.1, 0.25, 0.5, 0.75, 1 mg/mL C-NPs and positive control). (H) Cumulative DTX release study from the C-NPs. * $p < 0.05$, ** $p < 0.01$.

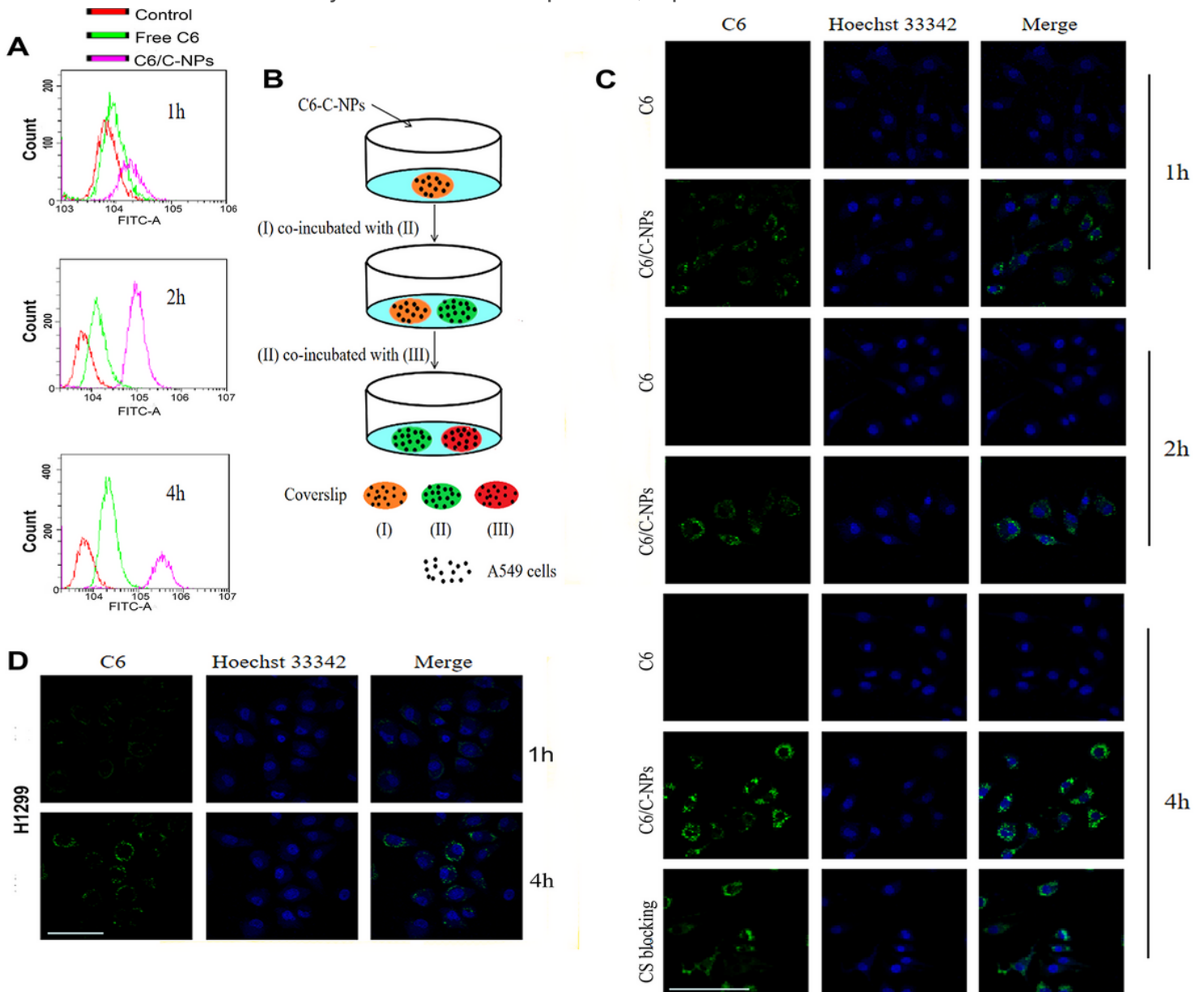


Figure 2

Cellular uptake efficiency as well as intracellular delivery results. (A) Flow cytometry analysis of free C6, C-NPs and C-NPs after CS blocking of A549 cells at incubating times. (B) Mechanism of intracellular uptake of C-NPs observed by CLSM. A549 cells on coverslip (I) were incubated in C6/C-NPs media for 4 h. Then coverslip (I) was washed, photographed, and placed together with coverslip (II) in a dish filled with fresh medium for 12 h. Later on, the process was repeated on coverslip (III). All results of three coverslips were demonstrated in Figure S4. Scar bars, 100 μ m. (C) Confocal microscopic observation of cellular uptake of A549 cells after incubating with different solutions. Scar bar, 100 μ m. (D) Images of H1299 cells with C-NPs at 1 or 4 h that were collected by CLSM. Scar bar, 100 μ m.

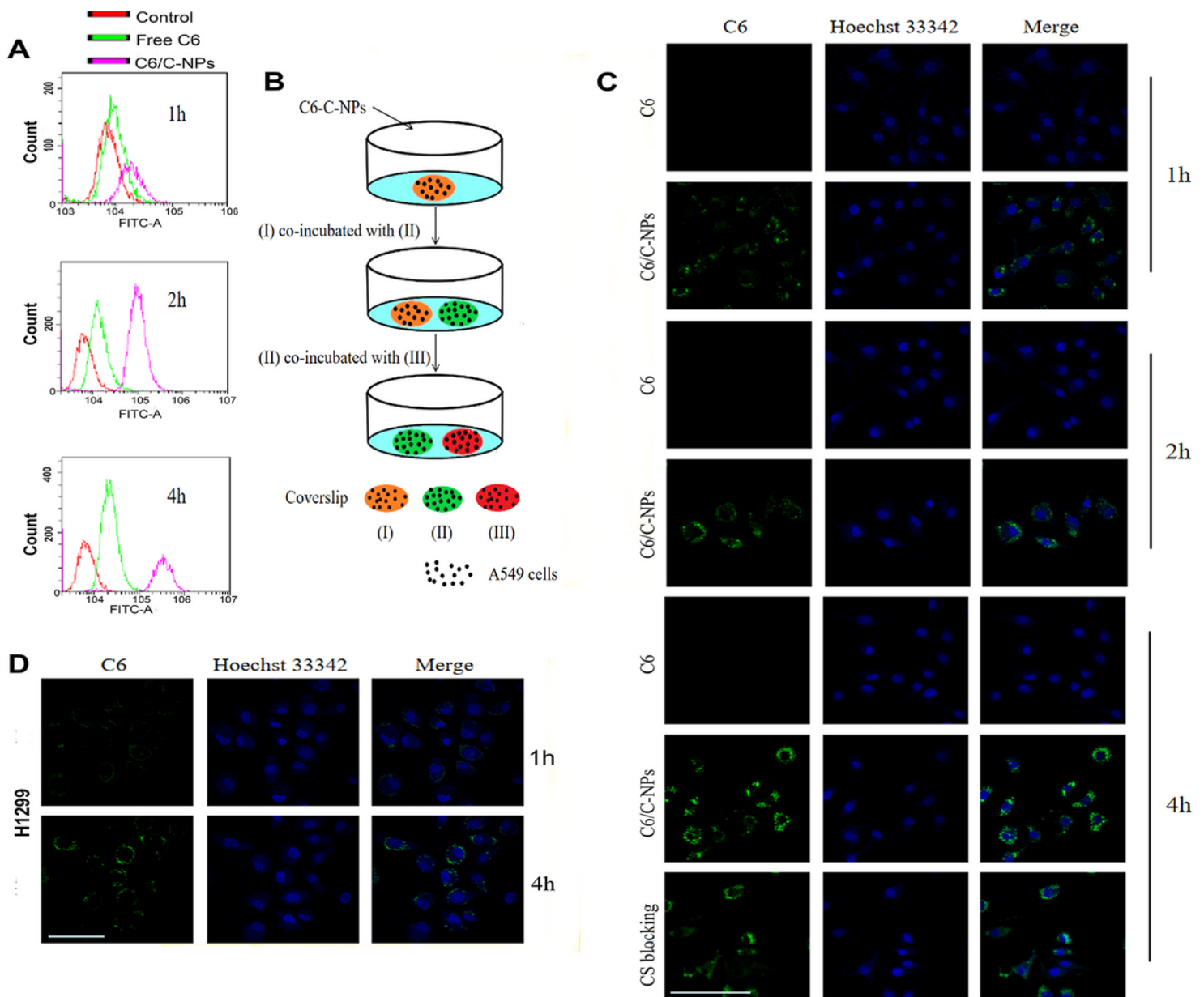


Figure 2

Cellular uptake efficiency as well as intracellular delivery results. (A) Flow cytometry analysis of free C6, C-NPs and C-NPs after CS blocking of A549 cells at incubating times. (B) Mechanism of intracellular uptake of C-NPs observed by CLSM. A549 cells on coverslip (I) were incubated in C6/C-NPs media for 4 h. Then coverslip (I) was washed, photographed, and placed together with coverslip (II) in a dish filled with fresh medium for 12 h. Later on, the process was repeated on coverslip (III). All results of three coverslips were demonstrated in Figure S4. Scar bars, 100 µm. (C) Confocal microscopic observation of cellular uptake of A549 cells after incubating with different solutions. Scar bar, 100 µm. (D) Images of H1299 cells with C-NPs at 1 or 4 h that were collected by CLSM. Scar bar, 100 µm.

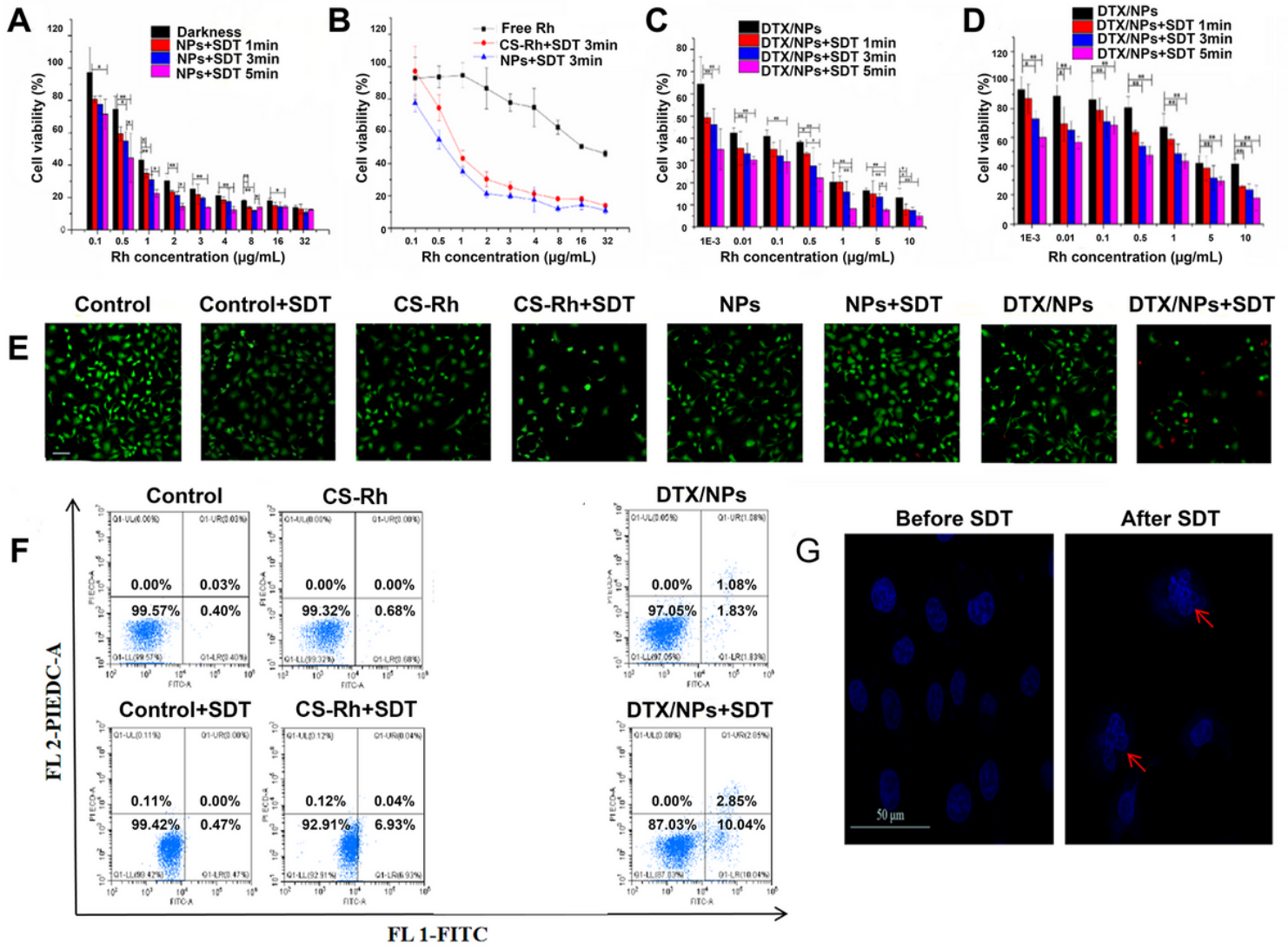


Figure 3

Different ways in assessing in vitro cytotoxicity and apoptosis. (A) Assessment results treating by C-NPs to A549 cells for acquiring cell viability at different concentrations in dark, and various ultrasonic time at 1.2 W/cm². (B) Assessment results treating by Rh, C-NPs and C-NPs with SDT to A549 cells for acquiring cell viability at different concentrations at 1.2 W/cm² for 3 min. (C) Assessment results treating by DTX/C-NPs to A549 cells and (D) H1299 cells for acquiring cell viability with or without SDT at different ultrasonic time at 1.2 W/cm². (E) Fluorescence images of live/dead cells using Calcein-AM and PI co-staining of A549. Scar bar, 50 μm . (F) Cell apoptosis results by FCM with different therapies. (G) Morphologies of cell nucleus before or after SDT therapy. Among this picture, *p < 0.05, **p < 0.01. Scar bar, 50 μm .

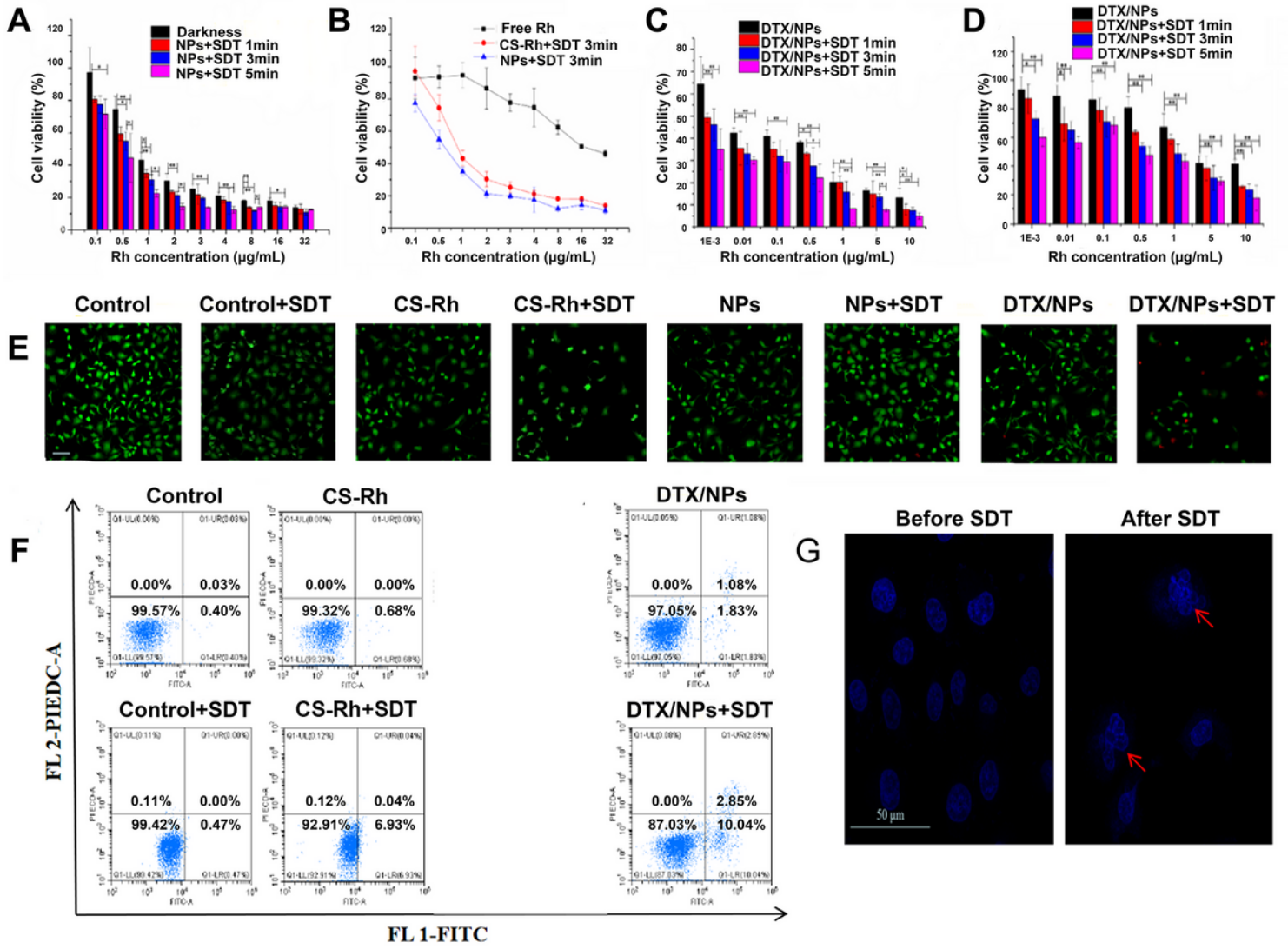


Figure 3

Different ways in assessing in vitro cytotoxicity and apoptosis. (A) Assessment results treating by C-NPs to A549 cells for acquiring cell viability at different concentrations in dark, and various ultrasonic time at 1.2 W/cm². (B) Assessment results treating by Rh, C-NPs and C-NPs with SDT to A549 cells for acquiring cell viability at different concentrations at 1.2 W/cm² for 3 min. (C) Assessment results treating by DTX/C-NPs to A549 cells and (D) H1299 cells for acquiring cell viability with or without SDT at different ultrasonic time at 1.2 W/cm². (E) Fluorescence images of live/dead cells using Calcein-AM and PI co-staining of A549. Scar bar, 50 μm . (F) Cell apoptosis results by FCM with different therapies. (G) Morphologies of cell nucleus before or after SDT therapy. Among this picture, *p < 0.05, **p < 0.01. Scar bar, 50 μm .

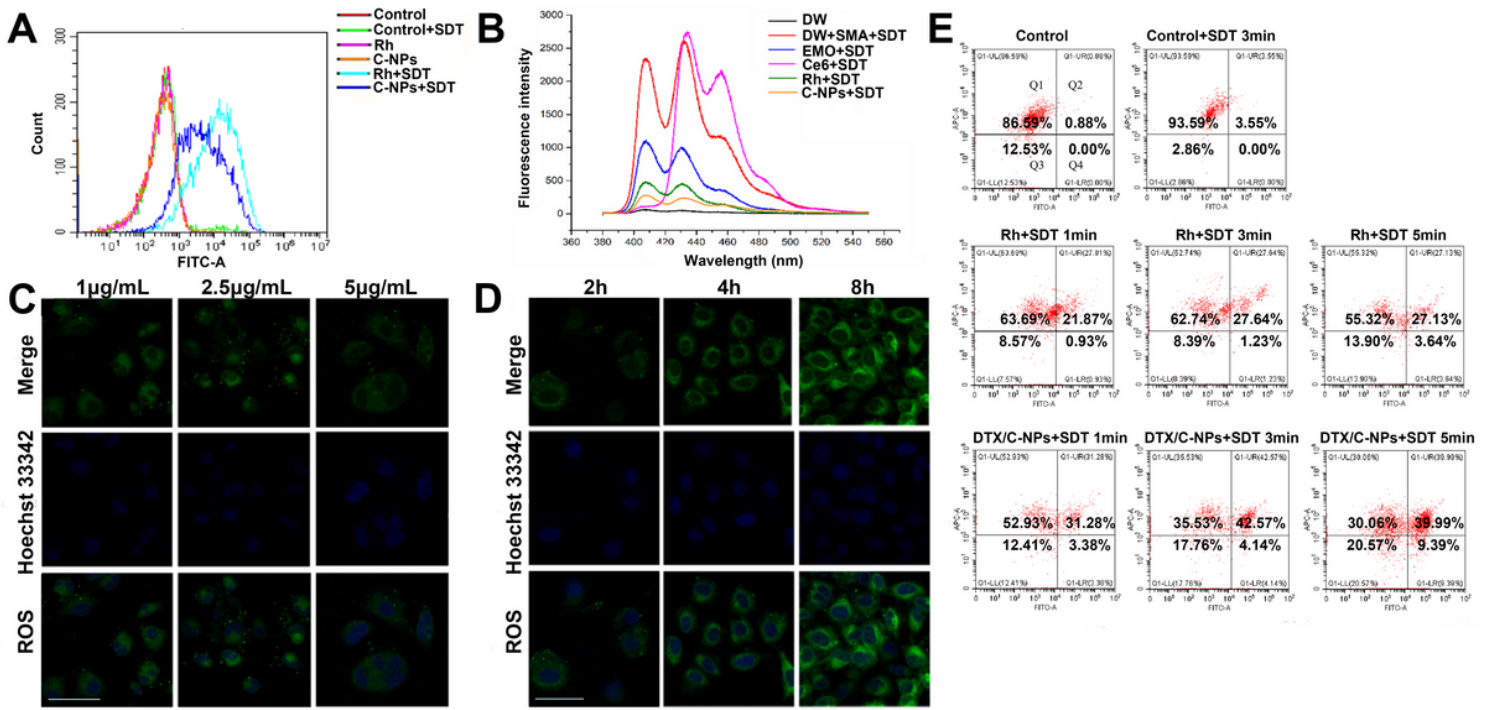


Figure 4

ROS production and MMP assessment. (A) FCM results of ROS generation assay in different solutions with/without SDT. (B) The productive ability of singlet oxygen was detected in various components with the aid of DMA after SDT treatment. ROS production was observed using a DCFH-DA probe by CLSM under (C) different concentrations of C-NPs (containing 1, 2.5 or 5 μ g/mL Rh) at the point of 12 h or (D) at different incubation times with fixed concentration of C-NPs (5 μ g/mL of Rh). Scar bar: 50 μ m. (E) MMP measurement result using a jc-1 probe. The y-axis represented the cells with normal MMP (red color) and transferred towards x-axis when the MMP decreased (green color).

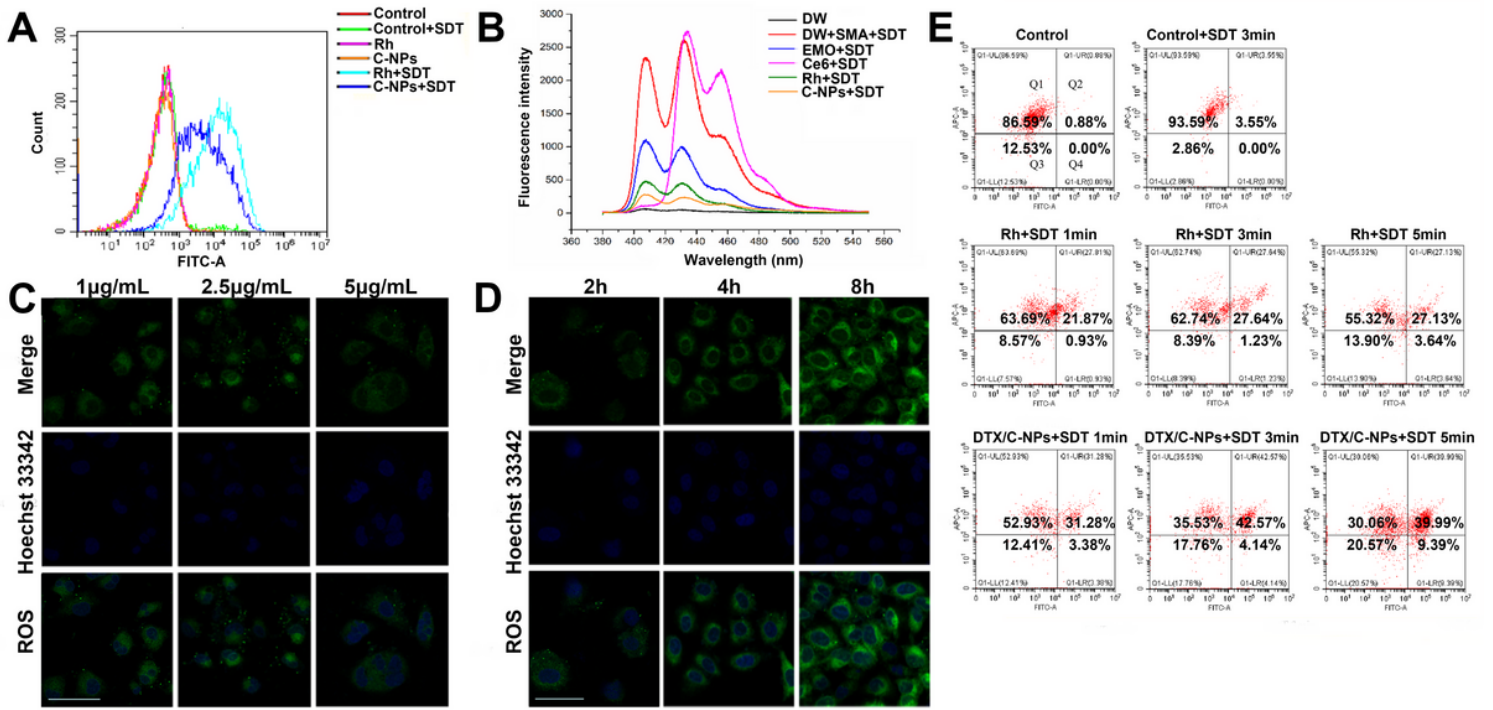


Figure 4

ROS production and MMP assessment. (A) FCM results of ROS generation assay in different solutions with/without SDT. (B) The productive ability of singlet oxygen was detected in various components with the aid of DMA after SDT treatment. ROS production was observed using a DCFH-DA probe by CLSM under (C) different concentrations of C-NPs (containing 1, 2.5 or 5 μ g/mL Rh) at the point of 12 h or (D) at different incubation times with fixed concentration of C-NPs (5 μ g/mL of Rh). Scar bar: 50 μ m. (E) MMP measurement result using a jc-1 probe. The y-axis represented the cells with normal MMP (red color) and transferred towards x-axis when the MMP decreased (green color).

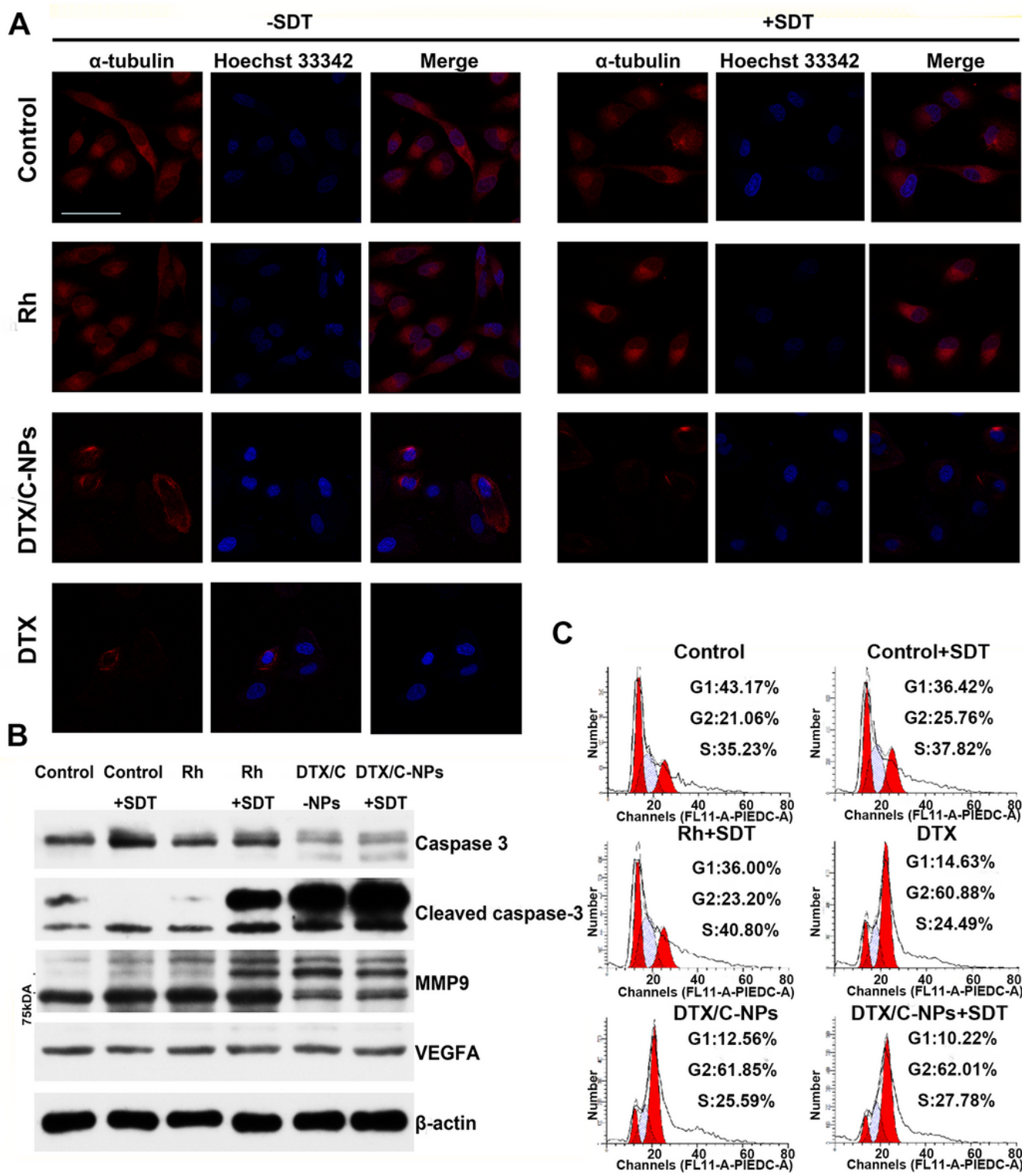


Figure 5

(A) A549 cells incubated with different solutions with/without SDT treatment were fixed and stained with α -tubulin (red) antibodies, fluorescence images were acquired by CLSM. Scar bar: 50 μ m. (B) Western Blot results. Expressions of caspase-3, cleaved caspase-3, MMP9 as well as VEGFA proteins after SDT treatment. (C) Cell cycle detection of A549 cells was measured using a kit after incubating with different solutions with/without SDT treatment.

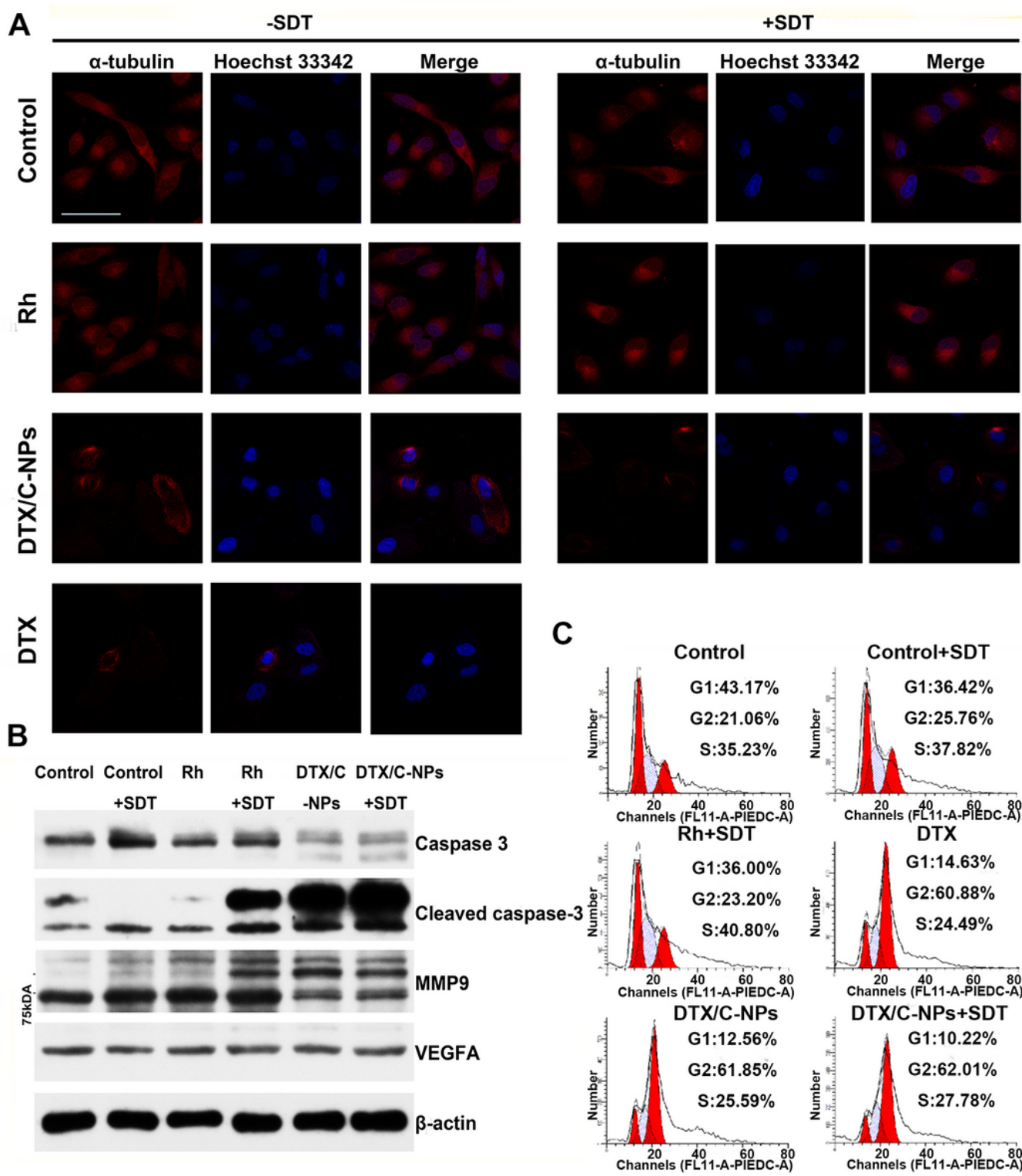


Figure 5

(A) A549 cells incubated with different solutions with/without SDT treatment were fixed and stained with α -tubulin (red) antibodies, fluorescence images were acquired by CLSM. Scar bar: 50 μ m. (B) Western Blot results. Expressions of caspase-3, cleaved caspase-3, MMP9 as well as VEGFA proteins after SDT treatment. (C) Cell cycle detection of A549 cells was measured using a kit after incubating with different solutions with/without SDT treatment.

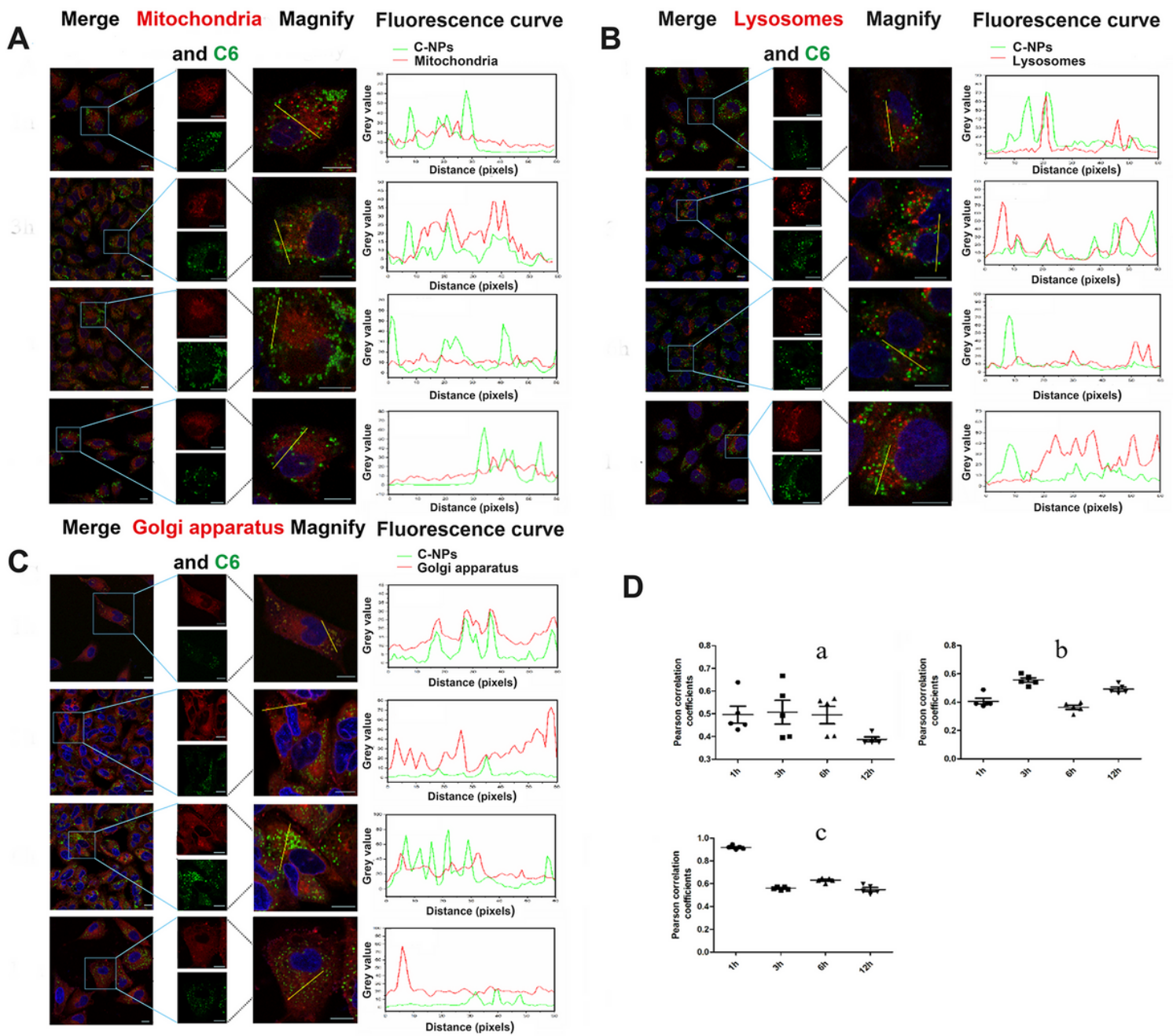


Figure 6

Distribution of C-NPs in several cytoplasmic organelles of A549 cells. The distribution of C6 from C-NPs in mitochondria (A), lysosomes (B) and Golgi apparatus (C) of A549 cells were observed by CLSM, and the pictures were taken and magnified for clearly observation. Besides, the fluorescence curves were depicted after drawing the corresponding thread. Scar bar, 10 μ m. (D) The Pearson correlation coefficient of C6 distribution in mitochondria, lysosomes and Golgi apparatus was calculated through Image J software.

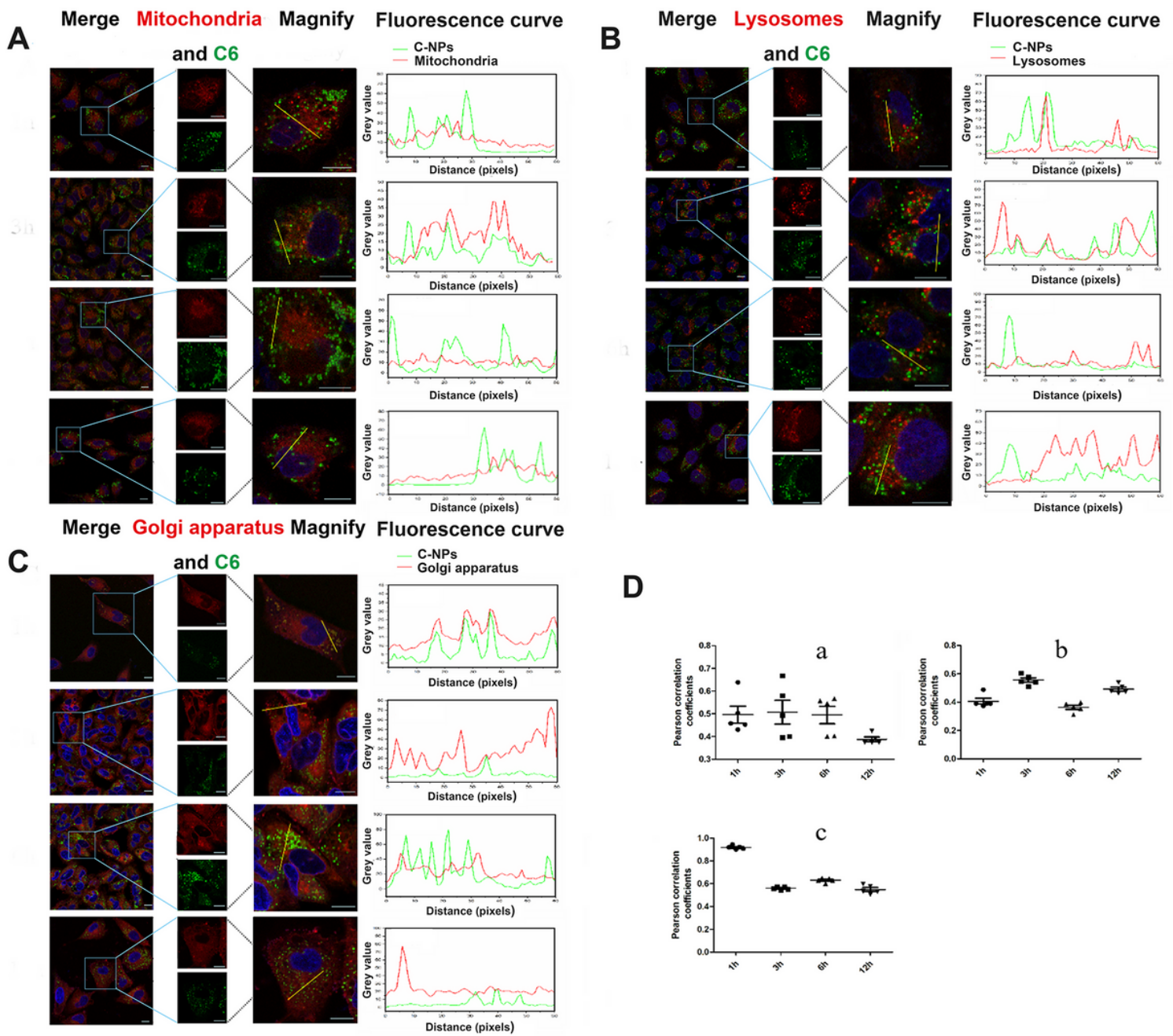


Figure 6

Distribution of C-NPs in several cytoplasmic organelles of A549 cells. The distribution of C6 from C-NPs in mitochondria (A), lysosomes (B) and Golgi apparatus (C) of A549 cells were observed by CLSM, and the pictures were taken and magnified for clearly observation. Besides, the fluorescence curves were depicted after drawing the corresponding thread. Scar bar, 10 μ m. (D) The Pearson correlation coefficient of C6 distribution in mitochondria, lysosomes and Golgi apparatus was calculated through Image J software.

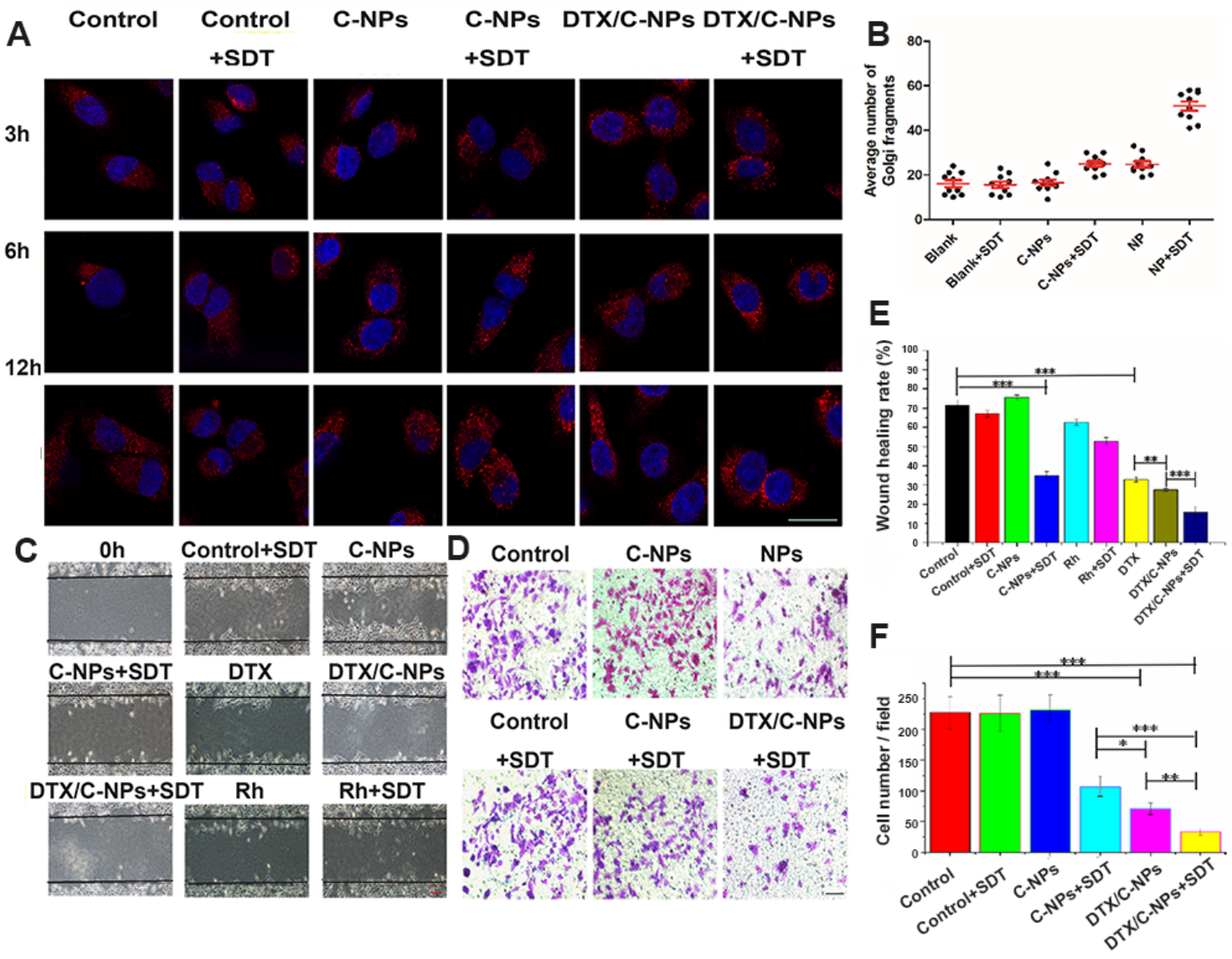


Figure 7

(A) Integrity of Golgi apparatus structure incubated with different dosages with/without SDT treatment was investigated by GM130 immunofluorescence assay (red) observed by CLSM at different times. Scar bar, 50 μ m. (B) Fragmented quantitation in Golgi apparatus for A549 cells after different treatment, and each dot represented the cell number from a single cell. (C) Wound healing ability of A549 cells incubated with different solutions with/without SDT for 24 h and observed by inverted fluorescence microscope. Scar bar, 50 μ m. (D) A549 cells crossing the transwell member were photographed by inverted fluorescence microscope. Scar bar, 50 μ m. The results of wound healing rate (E) and transwell assay (F) were both quantified by Origin 9.

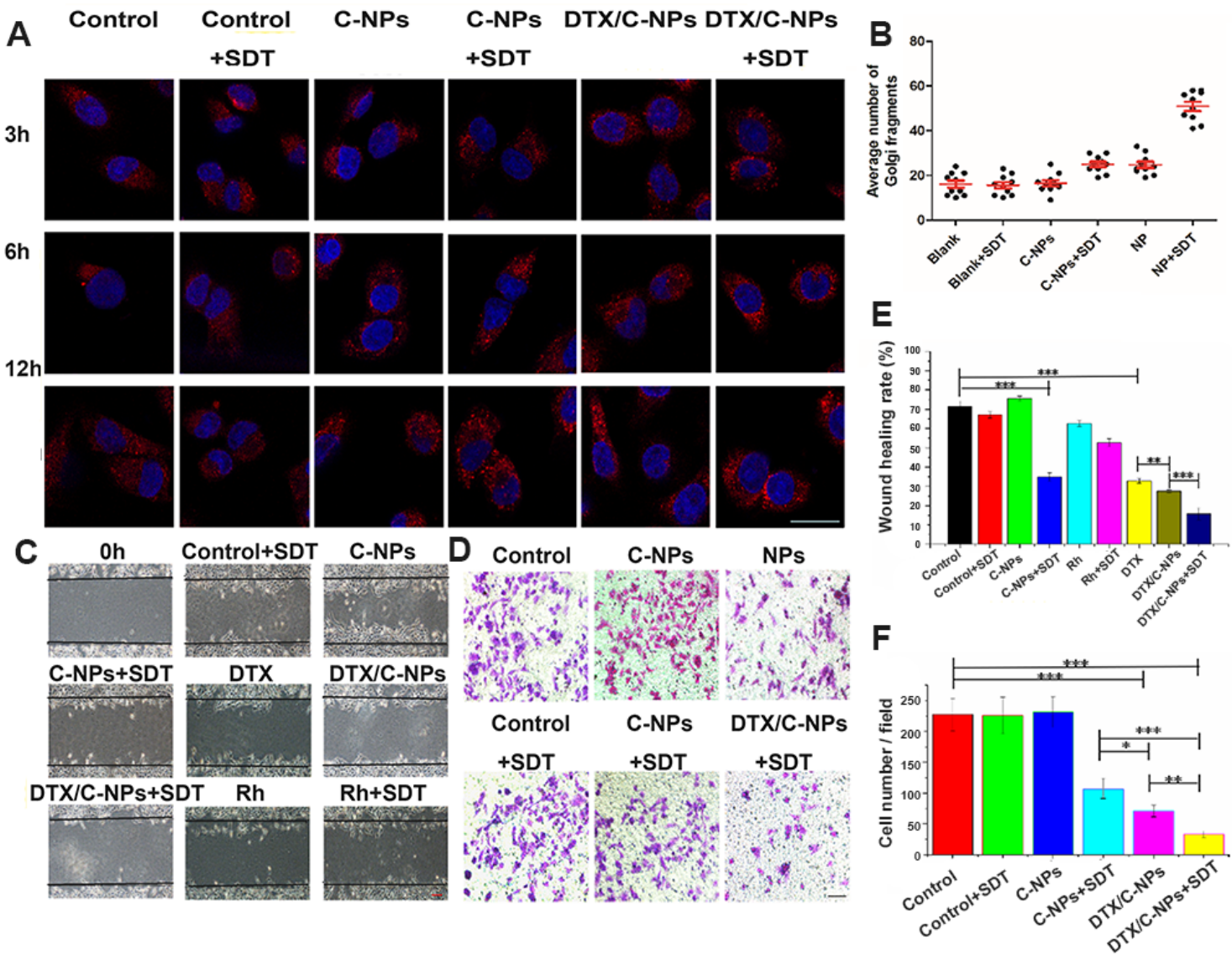


Figure 7

(A) Integrity of Golgi apparatus structure incubated with different dosages with/without SDT treatment was investigated by GM130 immunofluorescence assay (red) observed by CLSM at different times. Scar bar, 50 μ m. (B) Fragmented quantitation in Golgi apparatus for A549 cells after different treatment, and each dot represented the cell number from a single cell. (C) Wound healing ability of A549 cells incubated with different solutions with/without SDT for 24 h and observed by inverted fluorescence microscope. Scar bar, 50 μ m. (D) A549 cells crossing the transwell member were photographed by inverted fluorescence microscope. Scar bar, 50 μ m. The results of wound healing rate (E) and transwell assay (F) were both quantified by Origin 9.

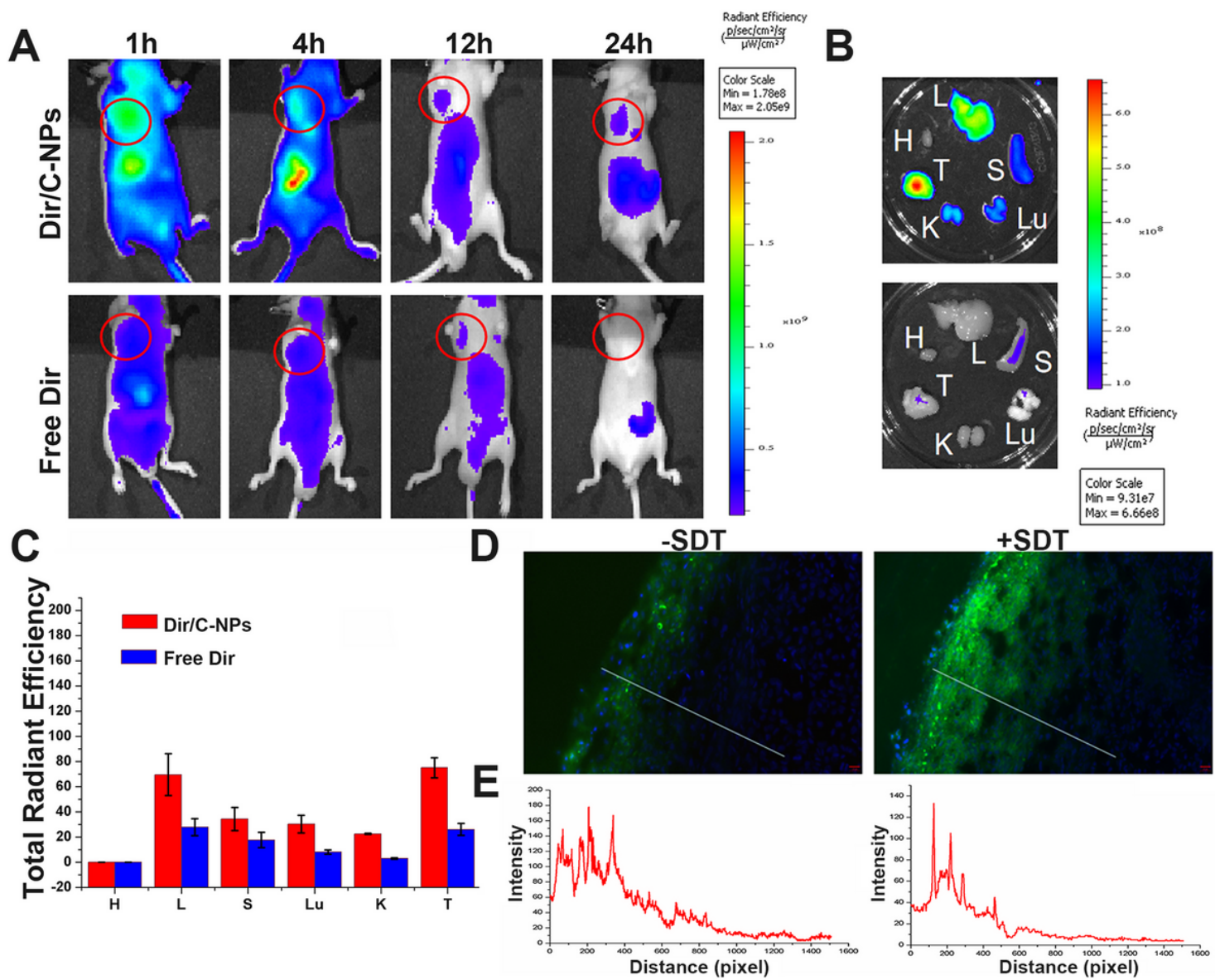


Figure 8

(A) Integrity of Golgi apparatus structure incubated with different dosages with/without SDT treatment was investigated by GM130 immunofluorescence assay (red) observed by CLSM at different times. Scar bar, 50 μm . (B) Fragmented quantitation in Golgi apparatus for A549 cells after different treatment, and each dot represented the cell number from a single cell. (C) Wound healing ability of A549 cells incubated with different solutions with/without SDT for 24 h and observed by inverted fluorescence microscope. Scar bar, 50 μm . (D) A549 cells crossing the transwell member were photographed by inverted fluorescence microscope. Scar bar, 50 μm . The results of wound healing rate (E) and transwell assay (F) were both quantified by Origin 9.

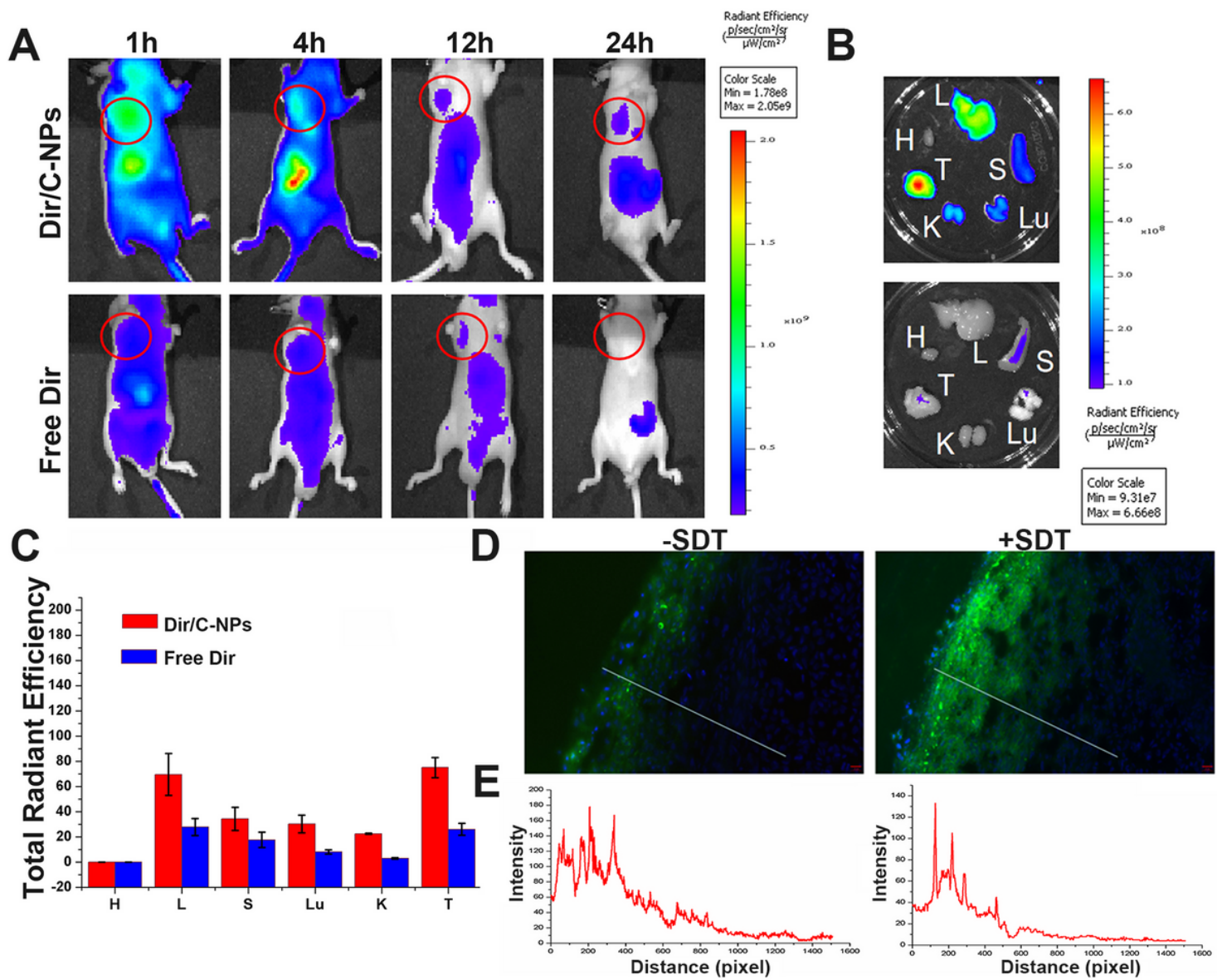


Figure 8

(A) Integrity of Golgi apparatus structure incubated with different dosages with/without SDT treatment was investigated by GM130 immunofluorescence assay (red) observed by CLSM at different times. Scar bar, 50 μm . (B) Fragmented quantitation in Golgi apparatus for A549 cells after different treatment, and each dot represented the cell number from a single cell. (C) Wound healing ability of A549 cells incubated with different solutions with/without SDT for 24 h and observed by inverted fluorescence microscope. Scar bar, 50 μm . (D) A549 cells crossing the transwell member were photographed by inverted fluorescence microscope. Scar bar, 50 μm . The results of wound healing rate (E) and transwell assay (F) were both quantified by Origin 9.

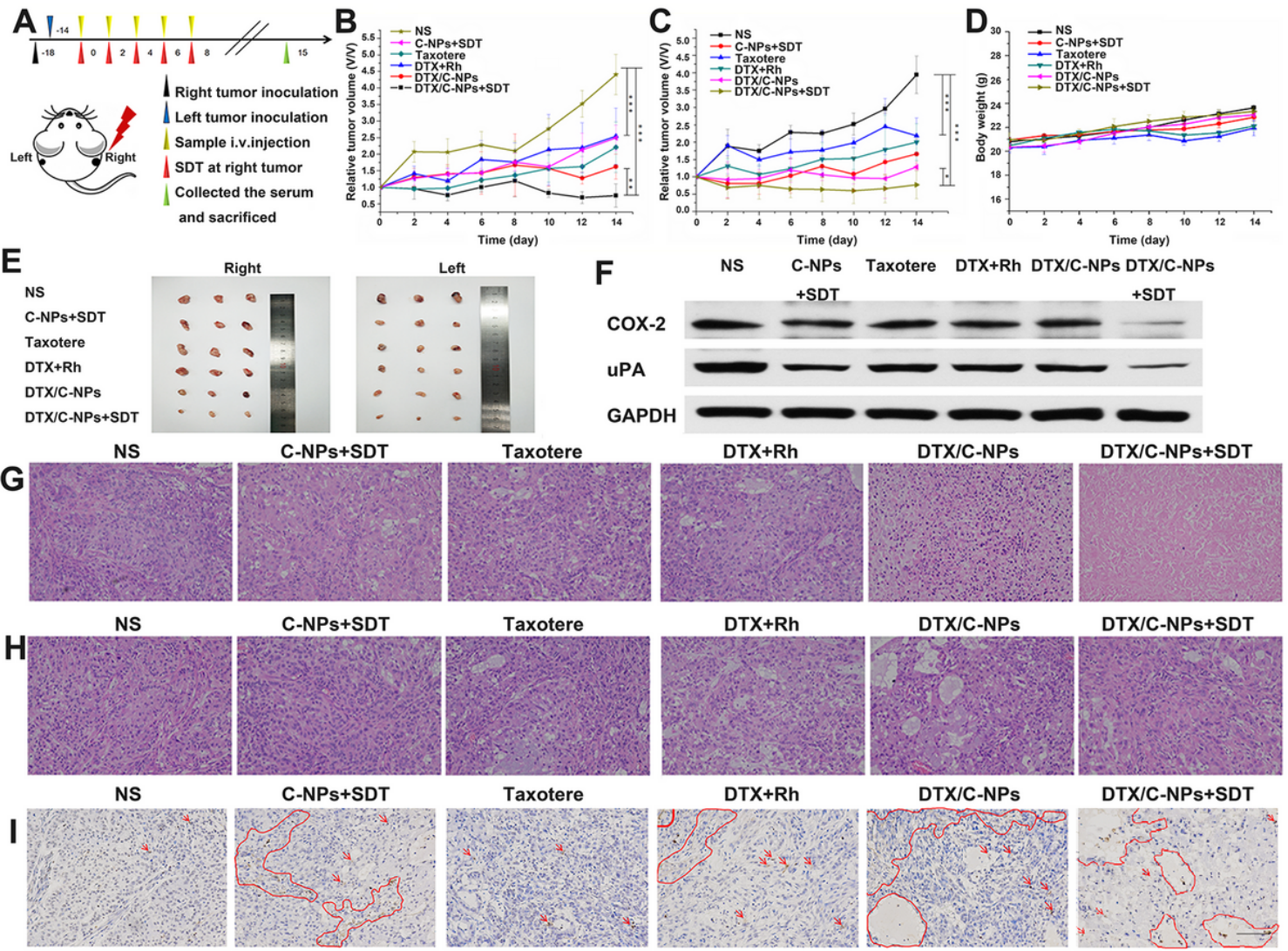


Figure 9

The summary of in vivo anti-tumor effect with bilateral A549 mice model. (A) Overall schedule of in vivo tumor inhibition study. RTV curves of 'R' (B) and 'L' (C) tumors and body weight curves (D). (E) Photographs of 'R' and 'L' tumors after the autopsy. (F) Western blot result of COX-2 and uPA proteins expression after treatment with different solutions at day 15. H&E stained images of 'R' (G) and 'L' (H) tumor tissues after the treatment with NS, C-NPs (SDT+), Taxotere, DTX + Rh, DTX/C-NPs (SDT+ or SDT-). Scar bar, 100 μ m. (I) TUNEL results of 'R' tumor from all bilateral tumor-bearing mice treated with NS, C-NPs (SDT+), Taxotere, DTX+Rh, DTX/C-NPs (SDT+ or SDT-). Scar bar, 100 μ m. **p < 0.01, ***p < 0.001.

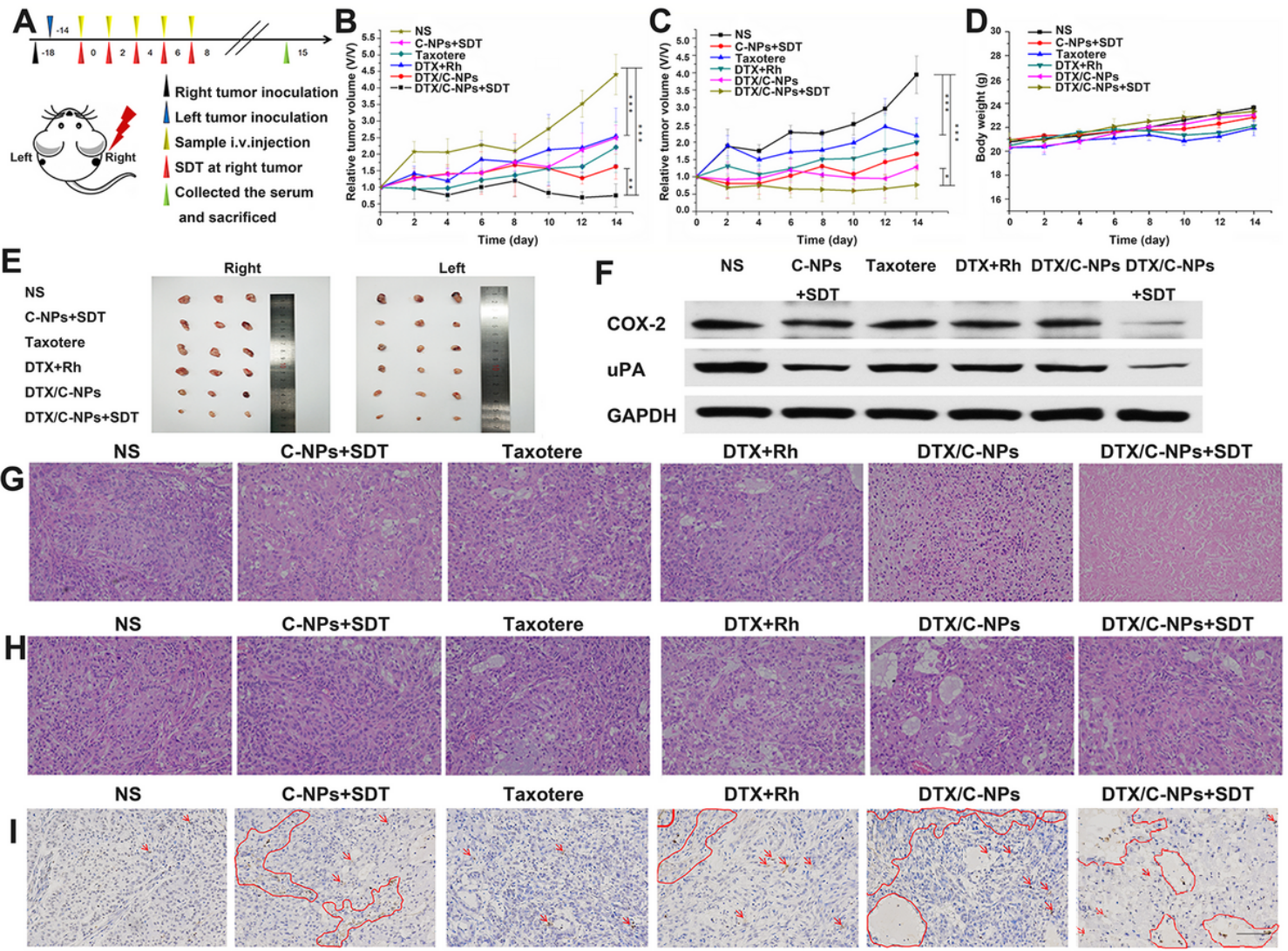


Figure 9

The summary of in vivo anti-tumor effect with bilateral A549 mice model. (A) Overall schedule of in vivo tumor inhibition study. RTV curves of 'R' (B) and 'L' (C) tumors and body weight curves (D). (E) Photographs of 'R' and 'L' tumors after the autopsy. (F) Western blot result of COX-2 and uPA proteins expression after treatment with different solutions at day 15. H&E stained images of 'R' (G) and 'L' (H) tumor tissues after the treatment with NS, C-NPs (SDT+), Taxotere, DTX + Rh, DTX/C-NPs (SDT+ or SDT-). Scar bar, 100 μ m. (I) TUNEL results of 'R' tumor from all bilateral tumor-bearing mice treated with NS, C-NPs (SDT+), Taxotere, DTX+Rh, DTX/C-NPs (SDT+ or SDT-). Scar bar, 100 μ m. **p < 0.01, ***p < 0.001.

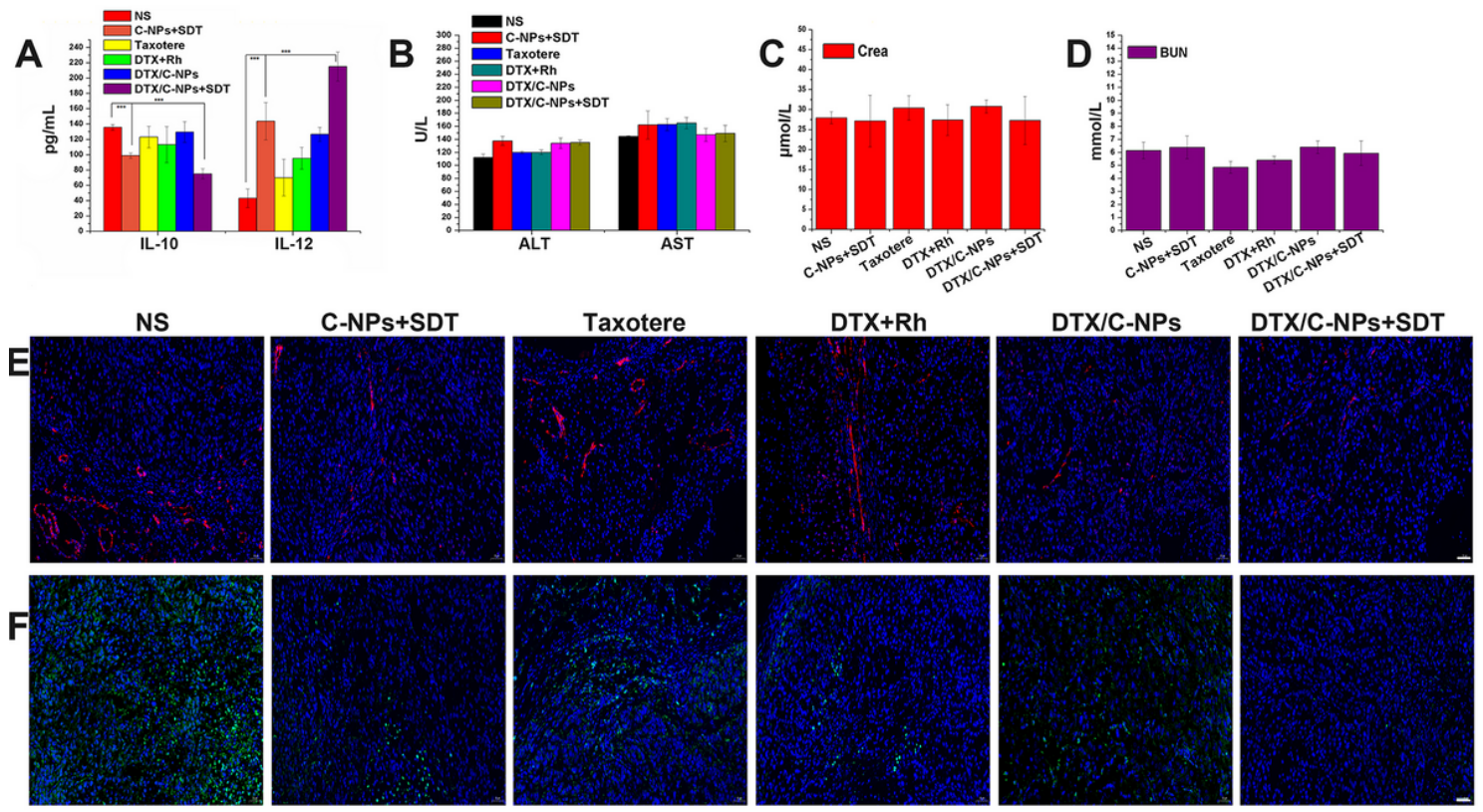


Figure 10

Serum composition determination and immunofluorescence results. The measurement of IL-10, IL-12 (A), ALT, AST (B), CREA (C) and BUN (D) in the mice serum after treating with NS, C-NPs+SDT, Taxotere, DTX+Rh, DTX/C-NPs and DTX/C-NPs+SDT. ***P < 0.001. Fluorescence images of anti-CD31-stained blood vessels (red fluorescence) (E), anti-CD206-stained M2 type macrophages (green fluorescence) (F) and DAPI-stained nuclei, respectively, by slices collected from Left tumors after different treatment. Scar bar, 50 μ m.

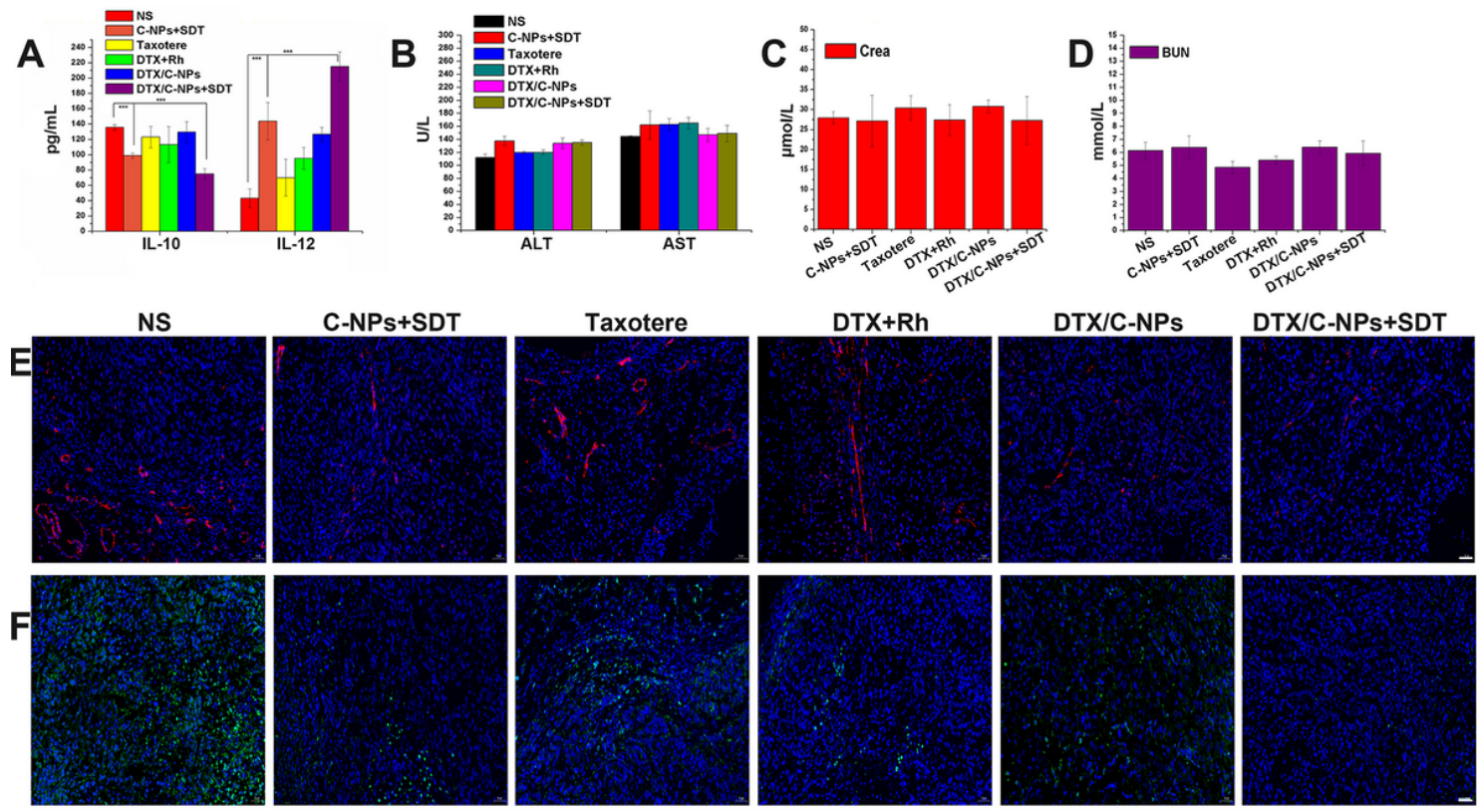


Figure 10

Serum composition determination and immunofluorescence results. The measurement of IL-10, IL-12 (A), ALT, AST (B), CREA (C) and BUN (D) in the mice serum after treating with NS, C-NPs+SDT, Taxotere, DTX+Rh, DTX/C-NPs and DTX/C-NPs+SDT. ***P < 0.001. Fluorescence images of anti-CD31-stained blood vessels (red fluorescence) (E), anti-CD206-stained M2 type macrophages (green fluorescence) (F) and DAPI-stained nuclei, respectively, by slices collected from Left tumors after different treatment. Scar bar, 50 μ m.

Supplementary Files

This is a list of supplementary files associated with this preprint. Click to download.

- Graphicalabstract.tif
- Graphicalabstract.tif
- CurvesandtableSection.docx
- CurvesandtableSection.docx
- supplement.docx
- supplement.docx